The Astrophysical Journal, 1004:226 (15pp), 2026 June 20 https://doi.org/10.3847/1538-4357/ae731c

From Nuclear Star Clusters to Little Red Dots: Black Hole Growth, Mergers, and Tidal Disruptions

Konstantinos Kritos[1] and Joseph Silk[1,2,3]

[1] William H. Miller III Department of Physics and Astronomy, Johns Hopkins University, 3400 North Charles Street, Baltimore, MD 21218, USA; kkritos1@jhu.edu

[2] Institut d'Astrophysique de Paris, UMR 7095 CNRS and UPMC, Sorbonne Université, F-75014 Paris, France

[3] Department of Physics, Beecroft Institute for Particle Astrophysics and Cosmology, University of Oxford, Oxford OX1 3RH, UK

Received 2025 October 23; revised 2026 March 29; accepted 2026 May 23; published 2026 June 16

Abstract

Little Red Dots, discovered by the James Webb Space Telescope, are hypothesized to be active galactic nuclei containing a supermassive black hole, possibly surrounded by a dense stellar cluster, large amounts of gas, and likely by a population of stellar-mass black holes. We develop a simple nuclear star cluster model to evolve the rapid mass growth of black hole seeds into the supermassive regime. The combined processes of tidal disruption events, black hole captures, and gas accretion are accounted for self-consistently in our model. Given the observed number density of Little Red Dots, and under reasonable assumptions, we predict at least a few tens of tidal disruption events and at least a few black hole captures at $z = 4$–6, with a tidal disruption event rate an order of magnitude larger than the black hole capture rate. We also estimate the uncertainties in these estimates. Finally, we comment on the low X-ray luminosity of Little Red Dots.

Unified Astronomy Thesaurus concepts: Star clusters (1567); Active galactic nuclei (16); Supermassive black holes (1663); James Webb Space Telescope (2291); Tidal disruption (1696)

1. Introduction

Nuclear star clusters (NSCs) are the densest systems observed in the local Universe with masses up to $10^8\,M_\odot$ (N. Neumayer et al. 2020). Studies have verified the relation between black hole (BH) mass and stellar velocity dispersion up to a redshift of $z \sim 9$, while the ratio of BH mass to stellar mass is higher beyond $z \gtrsim 2$ than in the local Universe by a factor of ∼10–100 (B. L. Jones et al. 2025a; I. Juodžbalis et al. 2025). Sometimes, the supermassive BH is heavier than the stellar component of the galaxy (R. Maiolino et al. 2026). This likely implies that the majority of the missing dynamical mass in star-depleted dark halos is in the form of baryonic gas, and that some massive BHs form early in gas-dominated dark halos (W. McClymont et al. 2026).

Strongly gravitationally lensed, high-redshift, dense star clusters have also been detected with the James Webb Space Telescope (JWST), with masses $\sim 10^6\,M_\odot$ and effective radii <1 pc (E. Vanzella et al. 2023; A. Adamo et al. 2024; L. Mowla et al. 2024), and reproduced in simulations (B. Polak et al. 2024; F. van Donkelaar et al. 2024; L. Mayer et al. 2025). These clusters hierarchically merge to form heavier NSCs in the centers of their dwarf galaxies (K. Fahrion et al. 2022). Simulations carried out by A. Rantala & T. Naab (2025) and N. Lahén et al. (2025) have demonstrated that intermediate-mass black hole (IMBH) seeds rapidly form in the centers of gas-rich star cluster complexes where the conditions resemble those in some high-redshift regions. Runaway stellar collisions rapidly form a very massive star within ∼1 Myr, which can collapse into an IMBH seed in metal-poor environments (M. C. Vergara et al. 2025). Cluster density controls the growth rate, while cluster mass controls the asymptotic mass value of the IMBH.

The diverse population of Little Red Dots (LRDs) discovered by the JWST at $z = 4$–6 suggests the high abundance of 10^7–$10^8\,M_\odot$ BHs at those redshifts and the BH masses measured assuming the local virial relations that connect the width of broad lines to BH mass (J. E. Greene et al. 2024; R. Maiolino et al. 2024a; J. Matthee et al. 2024). Some low-redshift LRD candidates have also been suggested with lower number densities in the local Universe (X. Lin et al. 2025; F. Loiacono et al. 2025). The absence of X-rays from all but a few LRDs is puzzling. It may indicate either high gas column densities near the accreting BH (A. de Graaff et al. 2025; K. Inayoshi & R. Maiolino 2025; X. Ji et al. 2025; R. Maiolino et al. 2025; R. P. Naidu et al. 2025) or lower BH masses (T. T. Ananna et al. 2024), or else that some LRDs could be in the form of accreting supermassive stars (M. C. Begelman & J. Dexter 2025; L. Zwick et al. 2026) or even be an extremely dense purely stellar system (J. F. W. Baggen et al. 2024). The high BH mass of $>10^7\,M_\odot$ is verified from resolved narrow-line kinematics by direct BH mass measurement in a strongly lensed LRD (I. Juodžbalis et al. 2026). Furthermore, F. Pacucci et al. (2025) suggest that the purely stellar interpretation for LRDs is problematic since the extremely high densities would inevitably lead to massive BH formation from collisional runaways. It is also indicated that a combined model of an accreting BH, a stellar population, and dense gas seems to better fit the spectral properties of LRDs (K. Inayoshi et al. 2025; B. Wang et al. 2025). LRDs are likely the places where SMBHs grew for the first time (K. Inayoshi 2025).

The presence of supermassive black holes (SMBHs) in the centers of LRDs may induce a cuspy distribution of stars around them, leading to increased tidal disruption events (TDEs; M. Rozner & E. Ramirez-Ruiz 2025). F. A. B. Garcia et al. (2025) have also argued that high-redshift NSC hierarchical formation may seed SMBHs and evolve into LRDs during the BH accretion phase.

We are not currently in a position to fully constrain the seeding mechanism of massive BHs at high redshift. However, the observations of BHs with a mass of up to $\sim 10^8\,M_\odot$ at redshift $z \sim 10$ (O. E. Kovacs et al. 2024; R. Maiolino et al. 2024b) and of inactive SMBHs (I. Juodžbalis et al. 2024) suggest that BHs likely grow through repeated bursts of super-Eddington episodes. This view is also supported by theoretical studies of BH growth models that compare with observational data from JWST and pulsar timing arrays (S. Bonoli et al. 2025; T. Zana et al. 2026).

We revisit the hypothesis that NSCs evolve dynamically into the observed high-redshift population of LRDs, assumed here to be highly compact and gas-rich galaxies containing massive central BHs (I. Labbé et al. 2023). A semianalytical framework is developed that includes loss-cone feeding, stellar evaporation, BH mergers, and gas accretion to form intermediate and even supermassive central BHs from plausible initial conditions.

Our key results are that early-forming NSCs, as motivated by theory (studies of merging trees to redshifts of ∼10 or higher; studies of low-metallicity star formation that favor clusters of $\sim 1000\,M_\odot$ stars) and observations of gravitationally lensed high-redshift compact star clusters, can provide a favorable environment for forming massive BHs at high redshift.

We predict enhanced and correlated rates of tidal disruptions in parallel with BH mergers and extreme-mass-ratio inspiral (EMRI) captures. Our estimated central massive BHs extend in mass to $\sim 10^7\,M_\odot$ in the first ∼100 Myr of the Universe, as well as at much later epochs in less extreme NSCs.

In what follows, we develop a model of NSC evolution and runaway BH formation, inspired by our earlier work (K. Kritos et al. 2023, 2024a). Section 2 contains a description of the best nearby proxy for LRDs, the Central Molecular Zone (CMZ) of the Milky Way galaxy (MWG), as a gas reservoir for the nuclear star cluster and SMBH at the Galactic center. We develop the physics of NSC evolution and BH growth in Section 3 using a semianalytic approach that rests on a relatively subjective choice of parameters. Our intent is to demonstrate what is possible in the context of conservative and more speculative assumptions, rather than to make precise predictions. We appeal to confirmation or otherwise of our inferred NSC evolution (Section 4), as well as our multimessenger predictions of TDEs and captured EMRIs (Section 5), which combine simple physics prescriptions with astrophysical uncertainties to justify the more extreme limits of our modeling. The X-ray predictions are described in Section 6, and we finally conclude in Section 7.

2. The CMZ and Nuclear Star Cluster as a Proxy for LRD Models

Our LRD modeling combines the stellar environment modeled by the massive equivalent of an NSC along with a substantial gas reservoir. To illustrate these initial conditions we use as a nearby proxy the MWG NSC and the surrounding CMZ as a less extreme counterpart. The local environment involves black hole mergers along with gas and stellar accretion—all crucial ingredients for our LRD model.

First, some definitions. The Bondi radius is defined as $GM_{\rm BH}/v_s^2$ where v_s is a generalized sound speed that includes turbulence, both supersonic and Alfvénic. The radius of the BH sphere of influence is $R_{\rm infl} = GM_{\rm BH}\sigma_\star^{-2}$. We use this definition for $R_{\rm infl}$ in this section as an order-of-magnitude estimate for the influence radius and in subsequent sections define it more accurately as the radius that contains a stellar mass of $2M_{\rm BH}$. We define $R_{\rm CMZ}$ as the extent of the gas reservoir in the CMZ of the MWG, and use the inner bulge of the MWG as a local template for an LRD. We use CMZ parameters taken from a recent review (J. D. Henshaw et al. 2023).

At high z, there is more gas. We expect in generic early CMZ regions that $M_{\rm gas}/M_\star \sim 0.1$–1 whereas $M_{\rm gas}/M_\star \sim 0.03$ for the MWG CMZ.

2.1. CMZ Properties

The properties of the CMZ are: radius 1 kpc, scale height 300 pc, gas density $n = 150\,{\rm cm}^{-3} = 1\,M_\odot\,{\rm pc}^{-3}$; $M_{\rm gas} \sim 3 \times 10^7\,M_\odot$; $\sigma_{\rm los} = 10\,{\rm km\,s}^{-1}$. The inflow rate from the bar is $\sim 0.1\,M_\odot\,{\rm yr}^{-1}$. For comparison, the MWG stellar bulge is nearly spherical with radius ∼2 kpc and mass $2 \times 10^{10}\,M_\odot$.

2.2. CMZ Components

The CMZ consists of, cumulatively, the “nuclear bulge” in the MWG that has the following components:

1. SMBH: $4 \times 10^6\,M_\odot$; the sphere of influence of Sgr A* is about 1 pc.
2. Nuclear star cluster, of mass $2.5 \times 10^7\,M_\odot$, size 1 pc; the sphere of gravitational influence of the NSC is about 30 pc.
3. CND: circumnuclear stellar disk. Gas mass $M_{\rm gas} = 3 \times 10^4\,M_\odot$. Size 1–7 pc. Gas density $n_{\rm H} = 10^{5-7}\,{\rm cm}^{-3}$. The line width is $\sigma_{\rm gas} = 10^4\,{\rm km\,s}^{-1}$. This contains the closest gas reservoir to Sgr A*.
4. NSD: nuclear stellar disk. Mass $10^9\,M_\odot$. Sphere of influence 300 pc. The NSD is cospatial with the CMZ.
5. Galactic stellar bar. Mass $1.9 \times 10^{10}\,M_\odot$. Sphere of influence 4 kpc. Found in 2/3 of nearby disk galaxies. Transports matter to CMZ by rotational torquing.

2.3. Current Star Formation Rate and Gas Flows in the CMZ

The star formation rate is $\sim 0.07\,M_\odot\,{\rm yr}^{-1}$. The star formation rate is bursty, separated by periods of 20–100 Myr, cf. Fermi bubbles. It is generated by a central explosion ∼50 Myr ago and initiated by central BH outflow and/or multiple supernovae. The gas inflow rate is driven by a bar and fuels the CMZ at $\sim 0.8\,M_\odot\,{\rm yr}^{-1}$. Further in, the inflow from the CMZ to the nucleus is $\sim 0.03\,M_\odot\,{\rm yr}^{-1}$. The observed gas line width due to turbulence is $12\,{\rm km\,s}^{-1}$. The inferred CMZ outflow rate, responsible for driving the Fermi bubbles, is $\sim 0.8\,M_\odot\,{\rm yr}^{-1}$. The ratio of gas outflow rate to star formation rate is ∼10. The accompanying supernova rate is $(2–15) \times 10^{-4}\,{\rm yr}^{-1}$.

2.4. CMZs in Distant Galaxies

CMZs are observed out to cosmic noon at $z \sim 2$. The gas velocity dispersion is $\sigma_{\rm gas} = 20$–$70\,{\rm km\,s}^{-1}$. The star formation rate is bursty. The inferred CMZ gas mass is of the order of the stellar mass or $\sim 10^9\,M_\odot$.

2.5. Schematic CMZ-based Model for an LRD

Consider a scaled-up early gas-rich version of the CMZ as a precursor of an LRD. It is compact due to strong gas cooling and turbulent transport of angular momentum. We expect that $M_{\rm gas} \sim M_\star$. We assume that the LRD is a very massive NSC with a central massive BH growing via BH mergers, TDEs, and gas accretion. The model assumes an early phase of super-Eddington accretion fed by Bondi accretion. Within the CMZ, we use dust-dominated cooling. The potential is dominated by the central massive BH inside its sphere of influence, given by $R_{\rm infl} = GM_{\rm BH}/\sigma_\star^2$. The corresponding infall timescale is $t_{\rm acc} = GM_{\rm BH}/\sigma_\star^3$ within the influence radius. We use the observed local scaling law: $M_{\rm BH} = 2\alpha\sigma_{200}^5 M_8$, where $M_8 = M_{\rm BH}/10^8\ M_\odot$, the stellar velocity dispersion $\sigma_{200} = \sigma/(200\,{\rm km\,s^{-1}})$, and the normalization constant α is of order unity. The gas reservoir is contained by the current Bondi radius, $R_{\rm B} = GM_{\rm BH}/v_s^2$. We equate this with $R_{\rm CMZ}$. Gas self-gravity traps gas within the influence radius, followed by freefall once $M_{\rm gas} \gtrsim M_{\rm BH}$. We use $M_8 = \alpha(\sigma_{200})^5$ to obtain $t_{\rm acc} = GM_{\rm BH}\sigma_\star^{-3} = 3 \times 10^5 \times \alpha^{3/5}M_8^{2/5}$ yr. We define M_g as the gas mass within the Bondi radius: $M_g = R_{\rm B}\sigma_\star^2/G = M_{\rm BH}(\sigma_\star/v_s)^2$ and the Bondi timescale $t_{\rm Bondi} = Gv_s^3 M_{\rm BH}^{-1} M_g^2 v_s^3 \sigma_\star^{-6}$. The Bondi radius is identified with $R_{\rm CMZ}$ and we use $\rho_g = \sigma_\star^6 G^{-3} M_g^{-2}$ to obtain $t_{\rm Bondi} = GM_{\rm BH}^{-1} M_{\rm gas}^2 v_s^3/\sigma_\star^6 \propto 1/M_{\rm BH}$.

The duty cycle is $t_{\rm Bondi}/t_{\rm acc} = (v_s/\sigma_\star)^3 (M_g/M_{\rm BH})^2$ with $M_{\rm gas}$ identified as the mass of the CMZ. The Eddington ratio is $L_{\rm acc}/L_{\rm Edd}$ and is proportional to $M_{\rm BH}^{-1}$. Hence $L_{\rm Edd}$ is very large and $t_{\rm Bondi}$ is very short at early phases, so that BH growth is rapid.

3. Semianalytical Model for LRDs

We model galactic nuclei as a double power-law density profile for both stars with mass m_1 and stellar-mass black hole remnants with mass m_2, as a two-mass model. This choice is based partly on observations of the central regions of galaxies and partly because, as we show later, it leads to an analytical description of velocity and potential profiles, thus minimizing the use of numerical integration as much as possible. Other past works employ a semianalytical framework similar to ours (S. L. Shapiro 1977; Y. Zhou & X. G. Zhong 1990; V. I. Dokuchaev 1991; K. Kaur et al. 2025), but our model differs by including the stellar-mass BH population and captured EMRIs together with the stellar TDEs and episodes of gas accretion onto the central massive BH.

3.1. Stellar and Black Hole Mass Distributions

We denote by R_1 and R_2 the break radii of the stellar and black hole density profiles, and by n_1 and n_2 the values of the number density at the break radii, respectively. Moreover, α_1 and β_1 are the indices of the stellar power-law density for radii $r < R_1$ and $r > R_1$, respectively. Similarly, we define α_2 and β_2. We thus have

$$n_1(r) = \begin{cases} n_1\left(\dfrac{r}{R_1}\right)^{\alpha_1}, & r < R_1 \\ n_1\left(\dfrac{r}{R_1}\right)^{\beta_1}, & r \geqslant R_1 \end{cases} \tag{1}$$

and a similar expression for the density $n_2(r)$ of stellar-mass black hole remnants. We assume $\beta_1, \beta_2 < 0$ and $\alpha_1, \alpha_2 \leqslant 0$ so that densities vanish as $r \to \infty$, but allow the possibility of a flat density within the break radius. Such a broken-power-law two-mass model is a highly flexible and simple model that can describe a range of possible profile configurations, including both cored and cuspy nuclei. A broken power law is similar to the Nuker law, which adequately describes the central regions within $\sim$300 pc of early-type galaxies observed at low redshift (T. R. Lauer et al. 1995). In particular, it is observed that the central density transitions from a steeper outer to a shallower inner profile at the break radius. The NSC of the Milky Way is also fitted well by a broken power-law (R. Schödel et al. 2014).

The total number of stars enclosed within radius r can be computed by integrating $4\pi x^2 n_1(x)$ from 0 to r and is

$$N_1(r) = \frac{4\pi n_1 R_1^3}{\alpha_1 + 3} \times \begin{cases} \left(\dfrac{r}{R_1}\right)^{\alpha_1+3}, & r < R_1 \\ 1 + \dfrac{\alpha_1+3}{\beta_1+3}\left[\left(\dfrac{r}{R_1}\right)^{\beta_1+3} - 1\right], & r \geqslant R_1 \end{cases} \tag{2}$$

and similarly for $N_2(r)$. Moreover, the total stellar and black hole remnant masses contained within radius r are $M_1(r) = m_1 N_1(r)$ and $M_2(r) = m_2 N_2(r)$, respectively. Convergence of the total mass in the system as $r \to \infty$ is achieved only when $\beta_1 + 3 < 0$ and the asymptotic value becomes $M_1(r \to \infty) \to 4\pi n_1 m_1 R_1^3 (\beta_1 - \alpha_1)(\alpha_1 + 3)^{-1}(\beta_1 + 3)^{-1}$. Similarly, we require $\beta_2 + 3 < 0$ such that $M_2(r \to \infty) < \infty$ for the stellar-mass black hole subsystem.

3.2. Velocity Dispersion Profiles

If $M_{\rm BH}$ is the mass of the central massive black hole in the system, then the total mass enclosed within radius r is $M(r) = M_{\rm BH} + M_2(r) + M_1(r)$. The one-dimensional stellar velocity dispersion $\sigma_1(r)$ can be computed by integrating Jeans' equation (see Equation (3.58) of D. Merritt 2013):

$$n_1(r)\sigma_1(r)^2 = \int_r^\infty \frac{G}{x^2} M(x) n_1(x) dx \tag{3a}$$

$$= I_{B1}(r) + I_{11}(r) + I_{21}(r). \tag{3b}$$

Notice that this equation neglects the collision term in the Fokker–Planck equation; we assume the system is collisionless on the crossing timescale, which is orders of magnitude smaller than the relaxation time (but see S. C. Rose et al. 2023; S. C. Rose & M. MacLeod 2024 for the effect of stellar collisions in NSC environments). To compute the integral in Equation (3a), we decompose it into three terms associated with the contribution of the central massive black hole $I_{B1}(r)$, the self-gravity of the stars $I_{11}(r)$, and the contribution from the stellar-mass black holes $I_{21}(r)$. These terms are computed in closed-form expressions as

$$I_{\rm B1}(r)=\begin{cases} I_{B1}(R_1)+\dfrac{GM_{\rm BH}n_1}{R_1^{\alpha_1}}\times\begin{cases}\ln\dfrac{R_1}{r}, & \alpha_1-1=0\\ \dfrac{R_1^{\alpha_1-1}-r^{\alpha_1-1}}{\alpha_1-1}, & \alpha_1-1\neq 0\end{cases} & ,\, r<R_1\\ -\dfrac{GM_{\rm BH}n_1}{(\beta_1-1)R_1}\left(\dfrac{r}{R_1}\right)^{\beta_1-1}, & r\geqslant R_1\end{cases} \tag{4a}$$

$$I_{11}(r)=\begin{cases} I_{11}(R_1)+\dfrac{4\pi Gn_1^2m_1}{(\alpha_1+3)R_1^{2\alpha_1}}\times\begin{cases}\ln\dfrac{R_1}{r}, & \alpha_1+1=0\\ \dfrac{R_1^{2(\alpha_1+1)}-r^{2(\alpha_1+1)}}{2(\alpha_1+1)}, & \alpha_1+1\neq 0\end{cases} & ,\, r<R_1\\ \dfrac{4\pi Gn_1^2m_1R_1^2}{(\alpha_1+3)(\beta_1+3)}\left[\dfrac{\beta_1-\alpha_1}{\beta_1-1}\left(\dfrac{r}{R_1}\right)^{\beta_1-1}+\dfrac{\alpha_1+3}{2(\beta_1+1)}\left(\dfrac{r}{R_1}\right)^{2(\beta_1+1)}\right], & r\geqslant R_1\end{cases} \tag{4b}$$

and the equations for $I_{B2}(r)$ and $I_{22}(r)$ can be computed by replacing all indices "1" by "2" above. Moreover, the cross term is computed analytically as

$$I_{21}(r)=\begin{cases} I_{21}(R_{\min})+\dfrac{4\pi Gn_1n_2m_2}{(\alpha_2+3)R_1^{\alpha_1}R_2^{\alpha_2}}\times\begin{cases}\ln\dfrac{R_{\min}}{r}, & \alpha_1+\alpha_2+2=0\\ \dfrac{R_{\min}^{\alpha_1+\alpha_2+2}-r^{\alpha_1+\alpha_2+2}}{\alpha_1+\alpha_2+2}, & \alpha_1+\alpha_2+2\neq 0\end{cases} & ,\, r<R_{\min}\\ I_{21}(R_{\max})+\dfrac{4\pi Gn_1n_2m_2}{\alpha_2+3}\times\mathcal{I}_{21}(r), & R_{\min}\leqslant r<R_{\max}\\ -\dfrac{4\pi Gn_1n_2m_2R_2^3}{(\alpha_2+3)(\beta_2+3)R_1}\left[\dfrac{\beta_2-\alpha_2}{\beta_1-1}\left(\dfrac{r}{R_1}\right)^{\beta_1-1}+\dfrac{\alpha_2+3}{\beta_1+\beta_2+2}\dfrac{r^{\beta_1+\beta_2+2}}{R_1^{\beta_1-1}R_2^{\beta_2+3}}\right], & r\geqslant R_{\max}\end{cases} \tag{5a}$$

$$\mathcal{I}_{21}(r)=\begin{cases} \dfrac{R_2^3}{(\beta_2+3)R_1^{\alpha_1}}\times\left[(\beta_2-\alpha_2)\times\begin{cases}\ln\dfrac{R_1}{r}, & \alpha_1=1\\ \dfrac{R_1^{\alpha_1-1}-r^{\alpha_1-1}}{\alpha_1-1}, & \alpha_1\neq 1\end{cases}+\dfrac{\alpha_2+3}{R_2^{\beta_2+3}}\times\begin{cases}\ln\dfrac{R_1}{r}, & \alpha_1+\beta_2+2=0\\ \dfrac{R_1^{\alpha_1+\beta_2+2}-r^{\alpha_1+\beta_2+2}}{\alpha_1+\beta_2+2}, & \alpha_1+\beta_2+2\neq 0\end{cases}\right] & ,\, R_1\geqslant R_2\\ \dfrac{1}{R_1^{\beta_1}R_2^{\alpha_2}}\times\begin{cases}\ln\dfrac{R_2}{r}, & \beta_1+\alpha_2+2=0\\ \dfrac{R_2^{\beta_1+\alpha_2+2}-r^{\beta_1+\alpha_2+2}}{\beta_1+\alpha_2+2}, & \beta_1+\alpha_2+2\neq 0\end{cases} & ,\, R_1<R_2\end{cases} \tag{5b}$$

where $R_{\rm max}\equiv\max(R_1, R_2)$ and $R_{\rm min}\equiv\min(R_1, R_2)$. Finally, $\sigma_1(r)=\sqrt{[I_{B1}(r)+I_{11}(r)+I_{21}(r)]/n_1(r)}$. In the case $n_1=0$, we then write $\sigma_1(r)=0$. We can also write a similar set of equations for $\sigma_2(r)$, the one-dimensional velocity dispersion of stellar-mass black holes. Convergence of all $I\ldots(r\to\infty)$ requires $\beta_1+1<0$ and $\beta_2+1<0$.

3.3. Gravitational Potential

The total gravitational potential is $\Phi(r)=\Phi_\infty+\Phi_{\rm BH}(r)+\Phi_2(r)+\Phi_1(r)$ where Φ_∞ is its value as $r\to\infty$. It can be computed as a superposition of three contributions, due to the potential of the central massive black hole $\Phi_{\rm BH}(r)$, the stellar-mass black hole remnants, $\Phi_2(r)$, and the stars, $\Phi_1(r)$. The first contribution is written as

$$\Phi_{\rm BH}(r) = -\frac{GM_{\rm BH}}{r}. \tag{6}$$

The stellar contribution can be written as

$$\Phi_1(r) = -\frac{4\pi G m_1 n_1 R_1^3}{\alpha_1+3} \times \begin{cases} \dfrac{1}{R_1^{\alpha_1+3}} \times \begin{cases} \dfrac{R_1^{\alpha_1+2} - r^{\alpha_1+2}}{\alpha_1+2}, & \alpha_1+2 \neq 0 \\ \ln(R_1/r), & \alpha_1+2 = 0 \end{cases} & , r < R_1 \\ \dfrac{1}{\beta_1+3}\left[\dfrac{\beta_1-\alpha_1}{r} - \dfrac{\alpha_1+3}{\beta_1+2}\dfrac{1}{R_1}\left(\dfrac{r}{R_1}\right)^{\beta_1+2}\right], & r \geqslant R_1 \end{cases} \tag{7}$$

and a similar expression exists for $\Phi_2(r)$. We may set $\Phi_\infty = 0$ as long as $\beta_1 + 2 < 0$ and $\beta_2 + 2 < 0$.

3.4. Particle Evaporation Rates

The specific energy of a particle in the cluster is $\varepsilon(r) = \frac{1}{2}v^2 + \Phi(r)$ and the escape velocity at radius r is thus $v_{\rm e}(r) = \sqrt{-2\Phi(r)}$ determined by the condition that a marginally escaping particle has zero energy. Particles with a velocity that exceeds this escape speed at radius r are removed from the system in one crossing time, which is given by $t_{\rm D}(r) = r/\sigma(r)$. Thus, if $p(v|\sigma(r))$ is the velocity distribution at radius r, assumed here to be a Boltzmann–Maxwell, then the fraction of stars with $v > v_{\rm e}(r)$ is

$$\begin{aligned} f_{\rm ev}(r) &= \int_{v_{\rm e}(r)}^{\infty} p(v|\sigma(r))dv \\ &= 1 - {\rm erf}\left[\frac{v_{\rm e}(r)}{\sqrt{2}\,\sigma(r)}\right] + \sqrt{\frac{2}{\pi}}\frac{v_{\rm e}(r)}{\sigma(r)}\exp\left[-\frac{v_{\rm e}(r)}{2\sigma(r)^2}\right] \end{aligned} \tag{8}$$

where erf and exp are the error and exponential functions, respectively. If we use $\sigma_1(r)$ ($\sigma_2(r)$) in Equation (8), then we obtain the fraction of stars (stellar-mass black hole remnants) that are moving at a velocity that exceeds the local escape speed at radius r. We further assume that the high-velocity tail ($v > v_{\rm e}$) of the velocity distribution is refilled via two-body relaxation as the primary mechanism. The two-body relaxation timescale for stars is given by

$$t_{R,1}(r) = \frac{0.34\sigma_1(r)^3}{G^2 n_1(r) m_1^2 \ln\Lambda_1} \tag{9}$$

where $\ln\Lambda_1 = \ln(0.5N_1(\infty))$ is the Coulomb logarithm. Thus, the evaporation rate of stars at radius r per unit star is given by

$$F_{\rm ev,1}(r) \equiv \frac{d\dot{N}_{\rm ev,1}(r)}{dN_1} = \frac{f_{\rm ev,1}(r)}{t_{\rm R,1}(r)}. \tag{10}$$

We can obtain the total evaporation rate of stars from the system by integrating Equation (10) over all radii and noting that $dN_1(r) = 4\pi r^2 n_1(r)dr$,

$$\dot{N}_{\rm ev,1} = \int_{r_{\rm min,1}}^{\infty} F_{\rm ev,1}(r) 4\pi r^2 n_1(r) dr \tag{11}$$

where $r_{\rm min,1}$ is the radius that contains a single star, i.e., determined by the condition $N_1(r_{\rm min,1}) = 1$.

Each time a particle is removed from the cluster, an amount of energy equal to the particle's energy is lost from the system. The fraction of energy per unit mass that is lost each relaxation time from radius r is

$$\begin{aligned} g_{\rm ev,1}(r) &= \int_{v_{\rm e}(r)}^{\infty} p(v|\sigma_1(r))\left[\frac{1}{2}v^2 + \Phi(r)\right]dv \\ &= \left(\frac{3}{2}\sigma_1(r)^2 + \Phi(r)\right) f_{\rm ev,1}(r) \\ &\quad + \frac{v_{\rm e}(r)^3}{\sqrt{2\pi\sigma_1(r)^2}}\exp\left[-\frac{v_{\rm e}(r)^2}{2\sigma_1(r)^2}\right]. \end{aligned} \tag{12}$$

We compute the total energy loss rate at radius r per unit star as $G_{\rm ev,1}(r) \equiv m_1 g_{\rm ev,1}(r)/t_{\rm R,1}(r)$, and the total energy loss rate from the stellar system due to evaporation is

$$\dot{E}_{\rm ev,1} = \int_{r_{\rm min,1}}^{\infty} G_{\rm ev,1}(r) 4\pi r^2 n_1(r) dr. \tag{13}$$

We implement a similar set of expressions to compute the stellar-mass BH number and energy evaporation rates, $\dot{N}_{\rm ev,2}$ and $\dot{E}_{\rm ev,2}$, respectively, where we replace all indices "1" by "2" in the equations above. Since stars and stellar-mass BHs have different velocity dispersions due to their distinct density profiles and masses, their evaporation rates are thus distinct.

3.5. Central BH Brownian Motion

The massive BH in the center will not be sitting motionless at $r = 0$, but will execute Brownian motion due to interactions with stellar-mass BHs and stars. It will thus have a velocity dispersion due to its wandering near the center, whose value is denoted by $\langle v_{\rm BH}^2\rangle$. Depending on whether it interacts more frequently with stars or stellar-mass BHs, the massive BH will be in equipartition with one or the other mass component, and thus $M_{\rm BH}\langle v_{\rm BH}^2\rangle$ will be equal to $3m_2\sigma_2^2$ or $3m_1\sigma_1^2$, respectively. We compute the rate of strong interactions (those that result in significant change in velocity during the encounter) of the massive BH with stars and stellar-mass BHs and take their ratio $\Gamma_1/\Gamma_2 \approx (n_1/n_2)(\sigma_2/\sigma_1)$ where densities and velocities are computed at their minimum radius because we assume the massive BH moves near the central region. Therefore, we write for the rms velocity of the massive BH,

$$\langle v_{\rm BH}^2\rangle^{1/2} = \sqrt{\frac{3}{M_{\rm BH}}} \times \begin{cases} \sigma_2(r_{\rm min,2})\sqrt{m_2}\,, & \Gamma_2 > \Gamma_1 \\ \sigma_1(r_{\rm min,1})\sqrt{m_1}\,, & \Gamma_1 > \Gamma_2 \end{cases} \tag{14}$$

as follows from kinetic energy equipartition (see Equation (5.127) of D. Merritt 2013). In particular, if stellar-mass BHs dominate the central region, then the wandering radius may be larger than if Brownian motion into the massive BH were caused solely by stars because typically $m_2\sigma_2^2 > m_1\sigma_1^2$ (H. B. Perets et al. 2007).

3.6. Accretion onto the Central BH

The presence of the massive BH in the center provides a sink for stars and BHs, which, if they approach close enough with a pericenter distance below a threshold value, are swallowed by the massive BH and are thus lost from the system. In contrast, evaporating particles are lost to infinity. We compute the tidal disruption event rate following the loss-cone formalism, as presented by D. Syer & A. Ulmer (1999). As for stellar-mass BHs captured by the central massive BH, we use the same loss-cone theory and substitute the tidal radius with the critical pericenter for gravitational-wave capture (see Equation (11) of G. D. Quinlan & S. L. Shapiro 1989). Since the tidal and capture radii increase nonlinearly with BH mass, we set the loss-cone radius to be either the tidal/capture critical pericenter distance or the horizon radius of the massive BH. We call these stellar-mass BHs captured by the central massive BH through the mechanism described “captured EMRIs.” These tend to have high eccentricities at formation and excite higher gravitational-wave harmonics (R. M. O’Leary et al. 2009).

We denote by $N_1 \equiv N_1(\infty)$ and $N_2 \equiv N_2(\infty)$ the total number of stars and stellar-mass BHs, respectively. Moreover, $M_1 = m_1N_1$ and $M_2 = m_2N_2$ are correspondingly the total masses. These numbers vary over time due to evaporation and loss-cone effects. We may write the time evolution of the total numbers as follows:

$$\dot N_1 = -\dot N_{\rm ev,1} - \dot N_{\rm lc,1} \tag{15a}$$

$$\dot N_2 = -\dot N_{\rm ev,2} - \dot N_{\rm lc,2}. \tag{15b}$$

As a consequence of the loss-cone effects associated with the consumption of stars and BHs, the mass of the central massive BH grows at a rate

$$\dot M_{\rm BH,lc} = f_{\rm lc,1}m_1\dot N_{\rm lc,1} + m_2\dot N_{\rm lc,2} \tag{16}$$

where $f_{\rm lc,1}$ is the fraction of the mass of the star accreted during a tidal disruption event, typically assumed to be 50% (M. J. Rees 1988).

Gas may be transported into the central parsec region of the galaxy from the larger kiloparsec scales. The process occurs in two steps (M. C. Sormani et al. 2023): first, from the galactic disk (kiloparsec scales) into the central molecular zone (∼100 pc) through dust lanes via which the gas is accreted and then funneled into the NSC. Inflow mechanisms that can drive gas into the nuclear region of the galaxy involve, among others, stellar feedback, magnetohydrodynamic turbulence, the presence of a bar structure, and extragalactic perturbations, such as those from satellites. Such a hierarchical inflow of gas toward the center through successive episodes of dynamical instability (the “bars-within-bars” channel) is one viable mechanism for fueling active galactic nuclei (AGN; I. Shlosman et al. 1989, 1990). More recently, multiscale simulations adopting the cyclic zoom-in method have demonstrated the feasibility for gas to be rapidly driven from galactic to horizon scales (M. Guo et al. 2025).

We expect the gas to be in a plasma state, due to stellar and radiation feedback from the central accreting BH. Furthermore, we take the gas uniformly distributed within the break radius of stars and compute the mean gas density as $\rho_{\rm g} = 3M_{\rm g}/(4\pi R_1^3)$.

The inflow rate can be computed from the freefall mass rate as $f_{\rm g}V^3/G$, where $f_{\rm g}$ is the gas mass fraction of the galaxy and V the circular velocity (K. Inayoshi et al. 2020). In turn, gas is accreted into the galaxy from the intergalactic medium. The gas must first accumulate into the Bondi sphere at the Bondi rate, become self-gravitating, and then collapse within a dynamical timescale $[(c_s^2 + \langle v_{\rm BH}^2\rangle)^{3/2}G^{-1}]$ to be accreted by the BH finally. Hyperaccretion is episodic; gas is subdominant in the dynamics of the cluster $M_{\rm g} \ll M_1, M_2$, and we ignore its contribution to the potential. We cap the gas accretion rate at a fixed Eddington ratio parameterized by the radiation efficiency $f_{\rm rad}$. The contribution of the gas accretion rate to the central BH’s mass is written as

$$\dot M_{\rm BH,g} = \min\left[\frac{4\pi\rho_{\rm g}(GM_{\rm BH})^2}{(c_s^2 + \langle v_{\rm BH}^2\rangle)^{3/2}}, \frac{(c_s^2 + \langle v_{\rm BH}^2\rangle)^{3/2}}{G}, \frac{0.1}{f_{\rm rad}}\frac{M_{\rm BH}}{t_{\rm Sal}}\right] \tag{17}$$

where $t_{\rm Sal} \approx 45.2$ Myr is the Salpeter timescale corresponding to a radiative efficiency of 10%. The radiative efficiency has a very low value within the photon trapping radius during super-Eddington accretion that can reach below 1% for Eddington ratios that exceed ∼10 (J. Poutanen et al. 2007). According to radiation-dominated magnetohydrodynamic simulations, the super-Eddington accretion phase can be sustained for several $10^4 \times GM_{\rm BH}/c^3$ and drives power outflows (L. Zhang et al. 2025).

We write the equation for the growth of the BH mass as the sum of the gas accretion and loss-cone contributions:

$$\dot M_{\rm BH} = \dot M_{\rm BH,lc} + \dot M_{\rm BH,g}. \tag{18}$$

Notice that the loss-cone growth term contains accretion of both stars and stellar-mass BHs (cf. (16)).

3.7. Energy Conservation Conditions

Let E_1 and E_2 be the total energies of the stellar and stellar-mass BH populations within their break radii, respectively. We compute the total stellar energy as

$$E_1 = \int_{r_{\rm min,1}}^{\infty}\left[\frac{3}{2}\sigma_1(r)^2 + \Phi(r)\right]4\pi m_1 n_1(r)r^2dr \tag{19}$$

and similarly for E_2. We compute the total rate of change of E_1 and E_2 by accounting for both heating rates from evaporation and loss-cone consumption. In addition, we assume that stellar-mass BHs serve as an energy source for the stars, as they have a higher temperature. The equations become

$$\dot E_1 = \dot E_{\rm ev,1} + \dot E_{\rm lc,1} \tag{20a}$$

$$\dot{E}_2 = \dot{E}_{\mathrm{ev},2} + \dot{E}_{\mathrm{lc},2}. \tag{20b}$$

Applying the chain rule, we also write these energy production rates as

$$\dot{E}_1 = \frac{\partial E_1}{\partial R_1}\dot{R}_1 + \frac{\partial E_1}{\partial R_2}\dot{R}_2 + \frac{\partial E_1}{\partial n_1}\dot{n}_1 + \frac{\partial E_1}{\partial n_2}\dot{n}_2 + \frac{\partial E_1}{\partial M_{\mathrm{BH}}}\dot{M}_{\mathrm{BH}} \tag{21a}$$

$$\dot{E}_2 = \frac{\partial E_2}{\partial R_1}\dot{R}_1 + \frac{\partial E_2}{\partial R_2}\dot{R}_2 + \frac{\partial E_2}{\partial n_1}\dot{n}_1 + \frac{\partial E_2}{\partial n_2}\dot{n}_2 + \frac{\partial E_2}{\partial M_{\mathrm{BH}}}\dot{M}_{\mathrm{BH}}. \tag{21b}$$

Moreover,

$$\dot{N}_1 = \frac{4\pi R_1^3}{\alpha_1 + 3} + \frac{12\pi n_1 R_1^2}{\alpha_1 + 3}\dot{R}_1 \tag{22}$$

and similarly for $\dot{N}_2$. We can combine all equations above to write a differential equation for $\dot{R}_1$ and $\dot{R}_2$. These equations become

$$\dot{R}_1 = \begin{cases} \dfrac{bf - ec}{D}, & D \neq 0 \\ \begin{cases} 0, & N_1 \leqslant 2 \\ \dfrac{c}{a}, & N_1 > 2 \end{cases}, & D = 0 \end{cases} \tag{23a}$$

$$\dot{R}_2 = \begin{cases} \dfrac{cd - af}{D}, & D \neq 0 \\ \begin{cases} 0, & N_1 \leqslant 2 \\ \dfrac{c}{b}, & N_1 > 2 \end{cases}, & D = 0 \end{cases} \tag{23b}$$

where we define

$$a \equiv \frac{\partial E_1}{\partial R_1} - \frac{3n_1}{R_1}\frac{\partial E_1}{\partial n_1} \tag{24a}$$

$$b \equiv \frac{\partial E_1}{\partial R_2} - \frac{3n_2}{R_2}\frac{\partial E_1}{\partial n_2} \tag{24b}$$

$$c \equiv \dot{E}_1 - \frac{\partial E_1}{\partial n_1}\frac{\dot{N}_1}{N_1} - \frac{\partial E_1}{\partial n_2}\frac{\dot{N}_2}{N_2} \tag{24c}$$

$$d \equiv \frac{\partial E_2}{\partial R_1} - \frac{3n_1}{R_1}\frac{\partial E_2}{\partial n_1} \tag{24d}$$

$$e \equiv \frac{\partial E_2}{\partial R_2} - \frac{3n_2}{R_2}\frac{\partial E_2}{\partial n_2} \tag{24e}$$

$$f \equiv \dot{E}_2 - \frac{\partial E_2}{\partial n_1}\frac{\dot{N}_1}{N_1} - \frac{\partial E_2}{\partial n_2}\frac{\dot{N}_2}{N_2} \tag{24f}$$

$$D \equiv bd - ae. \tag{24g}$$

3.8. Stellar-mass BH Binary Formation

We consider formation mechanisms for stellar-mass binary BHs related to two-body and three-body interactions. The former channel involves the strong interaction between two single stellar-mass BHs and the formation of a bound state following the efficient emission of gravitational waves along the hyperbolic encounter. The cross section for this process $\Sigma_{2\mathrm{b}}$ is given by Equation (4) of H. Mouri & Y. Taniguchi (2002), in which we set $m_i = m_j = m_2$. The volumetric rate density of two-body binary formation is given by $\gamma_{2\mathrm{b}} = n_2\langle\Sigma_{2\mathrm{b}}v_{\mathrm{rel}}\rangle$ where $\langle\ldots\rangle$ denotes average over the velocity distribution (assumed to be the Maxwell–Boltzmann) and $\langle v_{\mathrm{rel}}^2\rangle = 2\sigma_2^2$. The total two-body (2b) binary formation rate is

$$\Gamma_{2\mathrm{b}} = \int_{r_{\mathrm{min},2}}^{\infty} 12.1 c n_2(r)^2 \left(\frac{Gm_2}{c^2}\right)^2 \left(\frac{c}{\sigma_2(r)}\right)^{11/7} 4\pi r^2 dr. \tag{25}$$

The interaction of three single BHs can also lead to the formation of a bound state, and the volumetric formation rate density of surviving three-body binaries is given by $\gamma_{3\mathrm{b}} = 0.75 n_2^3 (Gm_2)^5/\sigma_2^9$ (J. Goodman & P. Hut 1993). The total three-body (3b) binary formation rate is obtained by integrating over the volume of the system:

$$\Gamma_{3\mathrm{b}} = \int_{r_{\mathrm{min},2}}^{\infty} 0.75 c n_2(r)^3 \left(\frac{Gm_2}{c^2}\right)^5 \left(\frac{c}{\sigma_2(r)}\right)^9 4\pi r^2 dr. \tag{26}$$

The total binary formation rate is then the sum of these two components, $\Gamma_{2\mathrm{b}} + \Gamma_{3\mathrm{b}}$.

4. Time Evolution of LRDs

Below we simulate two individual NSC examples with growing SMBHs. First, we show the initial conditions (Section 4.1) and time evolution of a typical NSC (Section 4.2) and later we consider a more compact and massive system (Section 4.3). For each system, we compare its evolution and the growth of the central BH with and without episodes of gas accretion. We compare the dependence of our results on the slope of the inner cusp in the Appendix.

4.1. Initial Conditions for a Typical NSC with an IMBH

We consider an NSC system with $n_1 = n_2 = 10^5\,\mathrm{pc}^{-3}$, $R_1 = 1\,\mathrm{pc}$, $R_2 = 0.2\,\mathrm{pc}$, $\alpha_1 = -0.5$, $\alpha_2 = -1.0$, and $\beta_1 = \beta_2 = -5.0$. The density, velocity dispersion, and loss-cone/evaporation rate profiles for this system are shown in Figure 1 and correspond to a snapshot of the system at $t = 0$.

The BHs consist of a subsystem more compact than the stellar population and dominate the density near the center. Motivated by simulations by T. Panamarev et al. (2019), we chose a stellar cusp shallower than the cusp formed by stellar-mass BH remnants; see also T. Alexander & C. Hopman (2009). The total mass of the system is about $10^6\,M_\odot$. The properties have been chosen to resemble the masses and radii of clusters observed at high redshift $z \sim 10$ (A. Adamo et al. 2024). At the center, a $10^3\,M_\odot$ BH seed is placed. The influence radii for the stellar and BH population are $\approx$0.1 pc and $\approx$0.04 pc, respectively, and correspond to the radii at which the total enclosed mass of each species is $2000\,M_\odot$. Moreover, the stellar distribution is expected to be cuspy around a massive BH (J. Frank & M. J. Rees 1976; M. Rozner & E. Ramirez-Ruiz 2025).

The IMBH seed at the center may have formed from an earlier phase of runaway stellar collisions, past rapid gas accretion, or direct collapse of a metal-poor cloud, or it may be of primordial origin. We are agnostic on its exact formation mechanism, and here we are concerned with the question of the subsequent mass growth of this intermediate-mass BH into the SMBH regime. See A. Escala (2021), M. C. Vergara et al. (2023), F. Pacucci et al. (2025), and A. Rantala & T. Naab (2025) for examples of

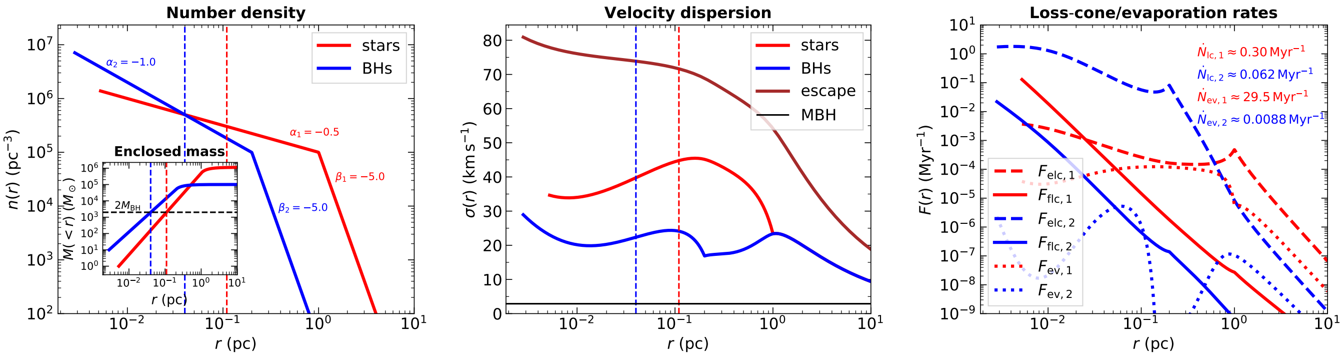

Figure 1. Radial profiles of number densities, total enclosed masses, velocity dispersions, and loss-cone and evaporation fluxes. Left: number density of stellar-mass BHs (blue) and stars (red). A massive BH with mass $M_{\rm BH} = 10^3\,M_\odot$ is placed in the center of the system. The blue and red vertical dashed lines correspond to the influence radii of BHs and stars, respectively. The inset shows the total mass of BHs (blue) and stars (red) enclosed within radius r. The horizontal black dashed line at $M(r) = 2M_{\rm BH}$ defines the influence radius. Middle: one-dimensional velocity dispersion for BHs (blue) and stars (red), as well as the escape velocity at radius r (brown curve). The horizontal black line represents the rms wandering velocity of the central massive BH. Right: full- and empty-loss-cone fluxes of BHs (blue solid and blue dashed curves) and stars (red solid and red dashed), as well as the evaporation fluxes of BHs (blue dotted) and stars (red dotted). Also shown in the upper right corner are the volume-integrated loss-cone and evaporation fluxes.

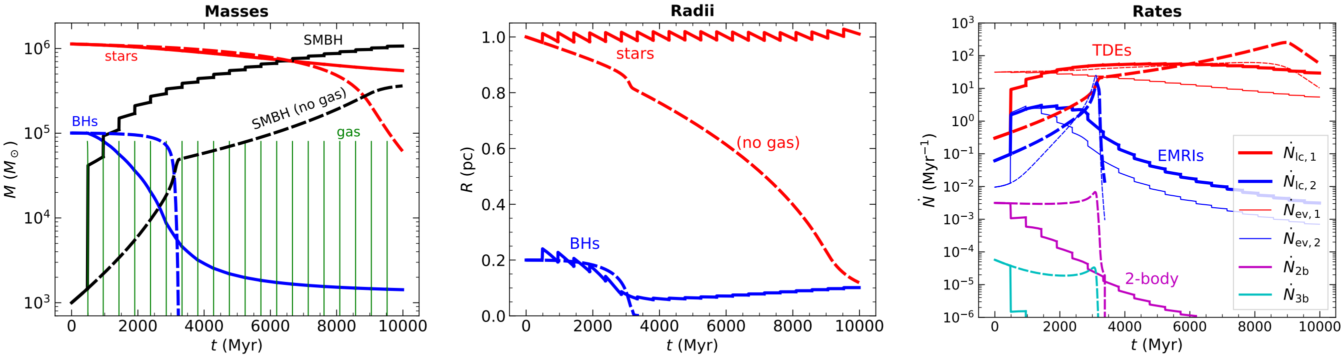

Figure 2. Time evolution of the system shown in Figure 1 with (solid) and without (dashed) gas accretion. In the former scenario, 20 gas inflow episodes, each of $8 \times 10^4\,M_\odot$ of gas, are added uniformly over time. Left: evolution of the total stellar mass (red), of the total mass in stellar-mass BHs (blue), and of the mass of the growing massive BH (black). The vertical green lines correspond to the episodes of gas inflow. Middle: evolution of the break radii of the stellar (red solid) and BH (blue solid) populations. Right: loss-cone (evaporation) rates for stars and BHs are the solid blue (thin solid blue) and solid red (thin solid red) lines, respectively. The magenta and cyan lines correspond to the formation rates of two-body and three-body stellar-mass binary BHs.

simulations of the collisional runaway scenario that produce $\sim 10^3\,M_\odot$ BH seeds in similar environments. S. Chon & K. Omukai (2025) discuss a direct collapse scenario in metal-enriched environments of a supermassive star that forms an IMBH of at least $\sim 10^3\,M_\odot$, and further fragmentation into dense star clusters with high star formation efficiencies is possible (B. Polak et al. 2024).

At a given radius within 1 pc stars have a larger velocity dispersion than BHs by a factor of a few. The discontinuity feature in the slope of $\sigma_2(r)$ at $r = R_2 = 0.2$ pc corresponds to an artificial effect caused by the choice of a break in the slope of the power law in the density profile and is not physical. In reality, the velocity dispersion is a smooth function of r. The escape velocity from the center takes its maximum value and is about $\sqrt{3} \times 80$ km s^{-1} $\simeq 140$ km s^{-1}. The three-dimensional rms velocity dispersion of the central intermediate-mass BH is $\simeq 4$ km s^{-1}. As a consequence, the wandering radius of the IMBH is small enough for it to be considered anchored to the center of the system. However, in our analysis, we do take into consideration the small value of the IMBH's velocity dispersion when computing TDE and captured EMRI rates.

In the right panel of Figure 1, we show the loss-cone and evaporation rate radial profiles for stars and BHs. For the parameters chosen in this example, at $t = 0$ all BHs are in the full-loss-cone regime while stars transition into the empty-loss-cone regime below the critical radius at $\simeq 0.02$ pc. Every 1 Myr about 30 stars are ejected from the system as a consequence of two-body relaxation, and the stellar evaporation flux peaks at a few $\times 0.1$ pc. The stellar-mass BH evaporation rate is ≈ 0.0088 Myr^{-1}. The central IMBH accretes one star every ≈ 3 Myr and one stellar-mass BH every ≈ 16 Myr from loss-cone effects.

4.2. Time Evolution of the Typical NSC

Next, we evolve the system presented above in time by numerically integrating Equations (22), (23), and (18). The system evaporates with time due to relaxation, and the central IMBH's mass grows by disrupting stars and capturing stellar-mass BHs. We consider two growth scenarios: one in which the BH grows solely through accretion, and another in which discrete phases of gas accretion are allowed to boost the mass of the BH.

The BH grows in mass initially primarily through capturing stellar-mass BHs. After the complete evaporation of the BH subsystem at $t \approx 3000$ Myr, the growth steadily proceeds through TDEs to finally reach an asymptotic value of $\approx 3 \times 10^5\,M_\odot$ (see Figure 2, left panel). Even though the TDE rate is higher than the BH capture rate by a factor of a few (see Figure 2, right panel), the BH mass growth is initially dominated by captured EMRIs because BHs are a factor of 10 heavier than stars. Furthermore, the gravitational-wave recoil kick obtained during the merger of the IMBH with $10\,M_\odot$ BHs is insignificant due to the significant mass asymmetry. Thus, the central BH is retained by the NSC.

The radius of the dry cluster decreases with time and reaches $\sim$0.1 pc by the end of the simulation. This is happening because as the BH grows, the central stellar velocity dispersion cusps and is $\propto R_1^{-1/2}$ while the total mass term changes by a smaller fraction.

Next, we consider 20 inflow episodes each of $8 \times 10^4\,M_\odot$ spread uniformly in time. The gas reservoir is $1.6 \times 10^6\,M_\odot$. We can safely neglect the impact of influence of gas on the dynamics because at each moment in time the gas contributes very little to the mass budget of the NSC. If a significant amount of gas inflows into the system and is rapidly removed, the result would be a significant expansion of the system (J. G. Hills 1980). This time, the BH's mass growth is boosted, and by the end of the simulation, the mass has grown to $>10^6\,M_\odot$. In our model, the accretion rate is higher with higher BH mass, and the feedback is proportional to the accretion rate. Thus, the duty cycle decreases as the BH's mass grows with time. In this example, the AGN lifetime shifts from $\sim$20 Myr down to less than $\sim$1 Myr throughout the simulation. Given that inflows occur every 500 Myr, the AGN duty cycle drops from $\sim$4% to about 0.1%.

The evolution of radius in the simulation with episodes of gas inflow exhibits a sawtooth-like appearance. This is attributed to adiabatic expansion during slow gas expulsion from the system, which happens each time a gas inflow episode occurs, followed by gas removal due to AGN feedback (J. G. Hills 1980). The gas thus prevents the system from collapsing, as in the dry case, and the break radius does not evolve significantly over 10 Gyr. Moreover, the BH subsystem does not totally evaporate, and a population of $\sim$1300 stellar-mass BHs survives after a Hubble time due to the effect of the gas.

In the initial snapshot, the stellar velocity dispersion is roughly flat. As the central massive BH grows, a stronger velocity cusp develops. At the final snapshot of the simulation at $t = 10$ Gyr, the velocity dispersion increases >100 km s^{-1} for radii <0.1 pc (see Figure 3). We verify that within the central region, the stellar velocity dispersion follows the $\sigma_1(r) \propto r^{-1/2}$ relation expected from a dominant central point-mass potential. Since the simulation, including gas inflow episodes, yields a more massive final SMBH, the velocity dispersion has a larger central value. In Figure 3, we also show for reference the central velocity dispersion profile around Sagittarius A*. We use data from Figure 12 of R. Schödel et al. (2009) and assume the Earth is at the galactocentric distance of 8 kpc. At $r \gtrsim 0.5$ pc the velocity dispersion in the Milky Way is roughly constant at the value $\approx$100 km s^{-1}, consistent with an isothermal density profile ($n \propto r^{-2}$). This differs from our predicted velocity dispersion profile at large distances, which continues to decrease due to a more rapid assumed decline in the mass density profile (r^{-5}). Nevertheless, this comparison is only qualitative since the simulated final properties of our NSC do not match those of the NSC at the center of the Milky Way. The Milky Way is perhaps the best example that exhibits a clear Keplerian rise near the center (D. Merritt 2013, chapter 1).

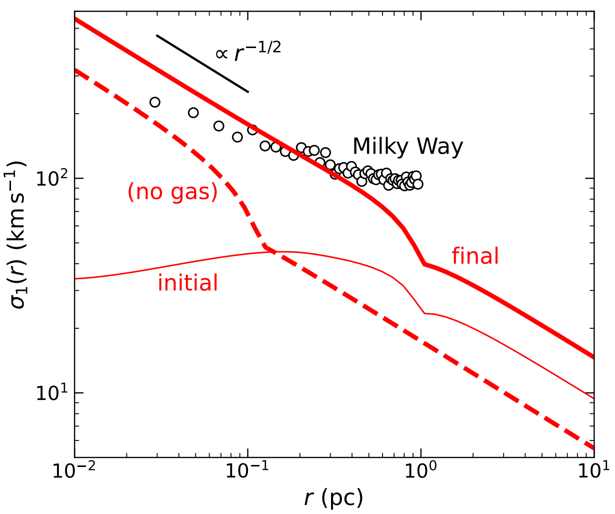

Figure 3. Snapshots of the stellar velocity dispersion profile at $t = 0$ (initial, thin line) and $t = 10$ Gyr (final) with (thick solid) and without (thick dashed) gas accretion episodes. The black line segment shows the radius-dependent Keplerian circular velocity. Finally, the black hollow circles correspond to Milky Way data from R. Schödel et al. (2009).

The timescale for the duration of a TDE fallback episode is given by Equation (4) of S. Gezari (2021). For solar-mass stars this TDE flare timescale is $t_{\rm TDE} \approx 0.11$ yr $M_6^{1/2}$ where M_6 is the mass of the central BH normalized to $10^6\,M_\odot$. We compute the TDE duty cycle as $t_{\rm TDE}\dot{N}_{\rm lc,1}$. The TDE duty cycle steadily increases from $\sim 10^{-8}$ to $\sim 10^{-5}$ in the first 5 Gyr and then to a maximum value of $\sim 10^{-4}$ at $t \sim 9$ Gyr, after which it drops by a factor of $\sim$3 by the end of the simulation. When we add gas inflows, the TDE duty cycle increases at a faster rate and then remains at higher values, approximately a few times 10^{-5}.

4.3. An Extremely Massive and Compact NSC Example

For our second example, we consider a denser version of the typical system we examined above. In particular, we set $n_1 = n_2 = 10^8$ pc^{-3} and choose stronger cusps, with $\alpha_1 = -1.0$ and $\alpha_2 = -1.5$ (close to a Bahcall–Wolf law with $\alpha = -1.75$). Furthermore, we take $R_1 = 4R_2 = 0.4$ pc. All other parameters are kept the same as in Section 4.1. We simulate this system for 100 Myr. The total initial mass of this NSC (including M_1, M_2, and $M_{\rm BH}$) is $\approx 10^8\,M_\odot$. We show a cartoon of our three-dimensional model for the NSC interpretation of LDRs in the left panel of Figure 4.

Observations of very dense clusters (A. Adamo et al. 2024) or very massive/compact galaxies (C. M. Casey et al. 2024), as well as simulations (A. Rantala et al. 2024; N. Lahén et al. 2025; C. E. Williams et al. 2025), hint at massive and compact environments like the one we consider in this subsection being already in place at high redshift ($z \gtrsim 10$).

In this case, the growth of the IMBH is more dramatic and a $\sim 10^7\,M_\odot$ SMBH emerges within a few $\times 10$ Myr (right panel of Figure 4). That is, the SMBH formation efficiency for this NSC—the final SMBH mass to initial total cluster mass as defined by M. C. Vergara et al. (2025)—is $\sim$10%. Moreover, the population of stellar-mass BHs does not dissolve on the simulated timescale, although $\approx$90% of the initial number of BHs is lost in either ejections or loss-cone effects. The corresponding loss fraction for stars is $\approx$2% on the same timescale.

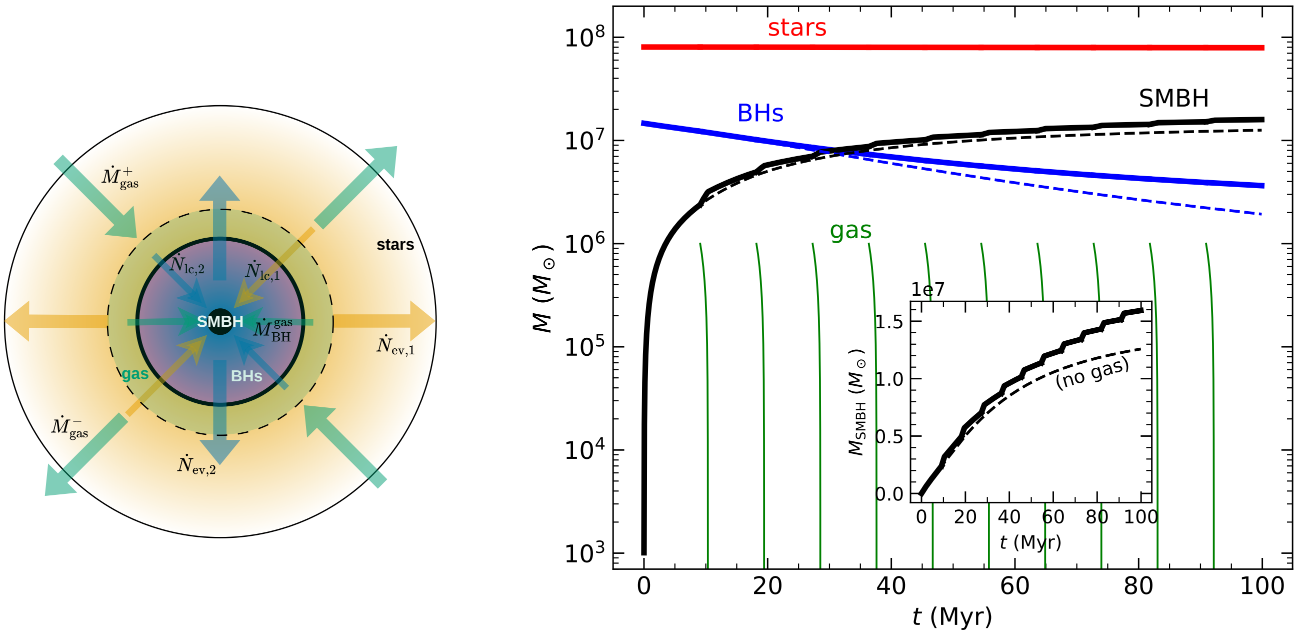

Figure 4. Left: cartoon of the spherical cluster model developed in this work. The outer diffuse orange region bounded by the solid black line corresponds to the bulk stellar population, and the inner blue overdensity bounded by the thick black line is the subcluster of stellar-mass BH remnants (BHs) in the core surrounding a supermassive BH (SMBH) represented by the central solid black sphere. The faint green dashed sphere indicates the presence of ionized hydrogen gas in the system. The thin inward (thick outward) arrows show the loss-cone influx (evaporation outflux) of stars $\dot{N}_{\rm lc,1}$ ($\dot{N}_{\rm ev,1}$) and BHs $\dot{N}_{\rm lc,2}$ ($\dot{N}_{\rm ev,2}$). Finally, the green inward and green outward thick arrows show the influx $\dot{M}^{+}_{\rm gas}$ and outflux $\dot{M}^{-}_{\rm gas}$ of gas from the system, while the green inward thin arrows $\dot{M}^{\rm gas}_{\rm BH}$ indicate gas accretion into the massive BH. Right: time evolution of the total stellar mass (red), total mass of stellar-mass BHs (blue), and mass of the massive BH (black). The dashed lines correspond to episodes of no gas inflow, while the solid green lines show gas inflow episodes. The inset shows the massive BH growth and the gas inflow episodes on a linear scale.

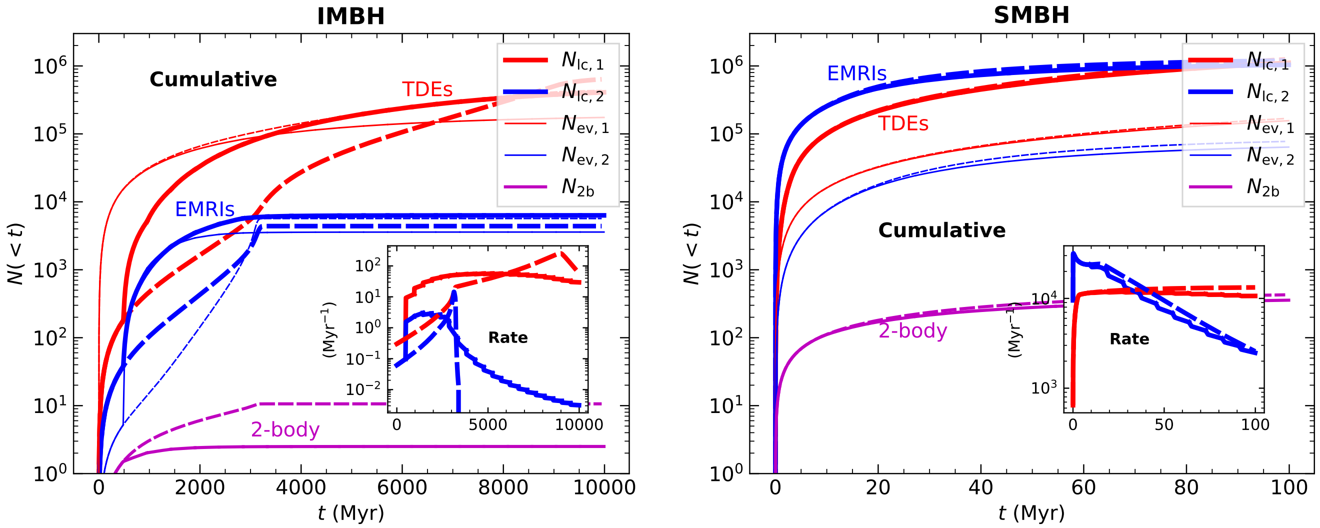

Figure 5. Cumulative number of tidal disruption events (TDEs), captured extreme-mass-ratio inspirals (EMRIs), and two-body binaries (2-body). Left: the cumulative numbers for the simulations of Figure 2. The inset shows the rates as a function of time, with the same x-axis as in the main plot. Right: correspondingly for the simulations of Figure 4. The cumulative number of three-body binaries is less than unity in both cases.

Over the 100 Myr simulated, one million TDEs and captured BHs occurred (see Figure 5, right panel). Hundreds of two-body binaries are formed between two stellar-mass BHs within the cusp around the SMBH. Most of these binaries are formed in the first 20 Myr with an initial peak rate of $\approx 70\ {\rm Myr}^{-1}$, which drops continually to a few ${\rm Myr}^{-1}$ at later times. The rates for three-body binary formation are at least two orders of magnitude smaller than the two-body rate. Thus, stellar-mass BH–BH merger rates from these two-body and three-body channels are expected to be low in environments similar to the one examined here.

We repeat the simulation for this system with the addition of ten gas inflow episodes every $\sim$9 Myr, each containing $10^6\ M_\odot$ of gas, assuming a gas reservoir of $10^7\ M_\odot$. This time, the AGN duty cycle is $\sim$10%, higher than in the previous example, and is maintained throughout the 100 Myr. With the addition of gas, the BH grows by an extra $\sim$30% compared to the growth it would have had via TDEs and captured EMRIs without the gas inflow episodes (see inset in Figure 4). A plausible scenario for LRDs would be the formation of the IMBH seed through runaway stellar collisions within a few Myr and the subsequent growth of the central BH through repeated TDEs, captured EMRIs, and gas accretion. Finally, the TDE duty cycle in this example is higher than in the previous one, it rises rapidly to a few percent within ∼10 Myr as the BH rapidly grows, and there is not much difference between the gas and gas-free cases.

5. Tidal Disruption Rates

In the previous section, we have presented the evolution of an NSC and the growth of its central massive BH through the combined effects of gas accretion, TDEs, and captured EMRIs. In this section, we estimate lower limits on cosmological TDE and EMRI rates based on the observed number density of LRDs at $z = 4$–6 and on properties of high-redshift star clusters detected with the JWST.

Based on the results by I. Juodžbalis et al. (2025), we assume that the $M_{\rm BH}$–$\sigma_\star$ relation holds up to redshift $z \sim 9$, where $\sigma_\star$ is the stellar velocity dispersion of the bulge. We use the relation from J. E. Greene et al. (2020). Up to an unknown fudge factor, we determine the break radius of the stellar density profile from the influence radius of the central SMBH, $R_1 = GM_{\rm BH}/\sigma_\star^2$. This is motivated by observations of low-redshift cored galaxies; see D. Merritt (2013), p. 20. Furthermore, based on standard assumptions regarding the initial mass function, the total mass in stellar-mass BHs is roughly ≈10% of the stellar mass, and assuming energy equipartition among stars and BHs, we estimate $R_2 = M_2R_1/M_1 \approx 0.1R_1$ (N. Choksi et al. 2019). Notice that if equipartition is not achieved, then BHs would undergo Spitzer instability, compactify even further, and have a smaller value for R_2 than what we estimate here, leading to an increase in captured EMRI rates.

We have used the constraints from Table 6 of J. Matthee et al. (2024) on the number density of LRDs in the SMBH mass range $\sim 10^7\,M_\odot$–$10^8\,M_\odot$. The measured number densities are provided for three SMBH mass bins $[10^{6.9}, 10^{7.3}]\,M_\odot$, $[10^{7.3}, 10^{7.7}]\,M_\odot$, and $[10^{7.7}, 10^{8.5}]\,M_\odot$, with corresponding number densities Φ_A, Φ_B, and Φ_C, respectively. Correspondingly given the rates per LRD as Γ_A, Γ_B, and Γ_C, we write the source-frame volumetric rate density as $R_s = \Phi_A\Gamma_A + \Phi_B\Gamma_B + \Phi_C\Gamma_C$. For simplicity, we assume this to be constant in the redshift range $z = 4$–6. Given the SMBH masses and the stellar velocity dispersions obtained from the $M_{\rm BH}$–$\sigma_\star$ relation, we determine the break radii of our LRDs to be in the range from a few parsecs up to 130 pc, which represents their observed compactness well.

Based on their global properties, the relaxation time of LRDs is greater than a Hubble time (A. Escala et al. 2025); however, presumably, their central NSCs are collisionally relaxed systems. We do not currently know, at the time of writing, the exact properties of putative NSCs in LRDs. We make some reasonable assumptions on the mass of NSCs when computing rates based on E. Vanzella et al. (2023), where massive compact clusters with masses $10^{6-7}\,M_\odot$ have been discovered at similar redshifts ($z \sim 6$). We thus use $10^6\,M_\odot$ or $10^7\,M_\odot$ as an educated guess for the mass of these systems.

The spin values of the SMBHs in the LRDs are also not known. However, under the assumption that these BHs have undergone significant accretion in the past, their spin is likely high, close to the extremal value, and spun up during the last mass doubling (J. M. Bardeen 1970). Low-redshift observations indicate that a substantial number of active SMBHs are spinning rapidly (dimensionless spin parameter $\gtrsim 0.5$), although there are still systematics in the techniques used in determining SMBH spin (C. S. Reynolds 2021). Moreover, the spin magnitude of BHs tends to decrease statistically and asymptote to zero through the repeated accretion of stars and BHs with random orientations (K. Kritos et al. 2024b, 2025b). Depending on the spin magnitude and orbital inclination of the approaching star, the Hills mass—the maximum mass of a BH that can tidally disrupt the star—can be up to several $\times 10^8\,M_\odot$ (A. Mummery 2023). For simplicity, we assume that all SMBHs in our examined mass range can produce an observable TDE. A more precise understanding of the SMBH spin distribution at $z \sim 5$ would enable us to estimate the Hills mass and thus the fraction of TDEs that produce an electromagnetic counterpart more accurately.

Once we compute the volumetric source-frame rate densities for TDEs and captured EMRIs, we integrate over comoving volume to obtain the observer-frame intrinsic cumulative yearly event rate of these transients in the redshift range $z = 4$–6. Under the assumption that R_s is constant in that redshift range we write (C. L. Rodriguez et al. 2016; A. Ricarte & P. Natarajan 2018)

$$\mathcal{R}_o = \int_{z=4}^{z=6} R_s \frac{1}{1+z} dV_c \approx R_s \int_4^6 \frac{dV_c}{dz}\frac{dz}{1+z}, \tag{27}$$

where the factor of $(1+z)^{-1}$ converts time from source frame to observer frame. We write $\mathcal{R}_o \approx (1.5 \times 10^{11}\,{\rm Mpc}^3) \times R_s$.

Since there is a range of predicted rates depending on initial conditions and the number density of LRDs, we report the 5%, 50%, and 95% percentiles, corresponding to pessimistic, median, and optimistic rates, respectively. We propagate errors in the LRD densities ($\Phi \pm \Delta\Phi$) and scatter in the $M_{\rm BH}$–$\sigma_\star$ relation into our predicted rates for TDEs and captured EMRI rates. We show our results in Tables 1 and 2, respectively.

With our choice of assumptions, we find a fixed ratio of $R_{\rm TDE}/R_{\rm EMRI} \sim 10{:}1$. Thus, for every captured EMRI, there are about ten stellar tidal disruption events happening at $z = 4$–6.

Table 1

The High-redshift ($z = 4$–6) Source-frame TDE Rate Density (R_s) from the Population of LRDs in Units of yr^{-1} Mpc^{-3} Calculated for the SMBH Mass Range $10^7\,M_\odot$–$10^8\,M_\odot$ and in Parentheses the Yearly Observer-frame Cumulative Number of TDEs ($\mathcal{R}_o$) in the Redshift Range $z = 4$–6

	TDE (yr^{-1} Mpc^{-3})	
Pessimistic	Median	Optimistic
6×10^{-13}	3×10^{-12}	2×10^{-11}
6×10^{-11} (8 yr^{-1})	2×10^{-10} (34 yr^{-1})	9×10^{-10} (133 yr^{-1})

Note. The first (second) row assumes LRDs contain a $10^6\,M_\odot$ ($10^7\,M_\odot$) star cluster. The three columns correspond to the pessimistic, median, and optimistic estimates.

Table 2

Same as Table 1 but for the Captured EMRI Rates

	Captured EMRI (yr^{-1} Mpc^{-3})	
Pessimistic	Median	Optimistic
6×10^{-14}	3×10^{-13}	2×10^{-12}
8×10^{-12} (1 yr^{-1})	4×10^{-11} (6 yr^{-1})	2×10^{-10} (31 yr^{-1})

The corresponding median volumetric source-frame TDE rate density is $R_{\rm TDE} \approx 0.003\,{\rm yr}^{-1}\,{\rm Gpc}^{-3}$ with an uncertainty of about 1 dex. This assumes an NSC mass scale of $10^6\,M_\odot$. If the typical mass of NSCs in those LRDs were $10^7\,M_\odot$, the TDE rate would be higher by a factor of $\sim$100. When integrated over the comoving volume (see Equation (27)), this results in a cumulative observer-frame TDE rate of $\approx 34\,{\rm yr}^{-1}$. Since we assume a fixed merger rate density over $z \in [4, 6]$, the same ratio of $\sim$10:1 holds for the volume-integrated observer-frame TDE and captured EMRI rates. This implies that only a few captured EMRIs occur every observer year at those redshifts.

LRDs represent the fraction of active SMBHs, and the difficulty in observing means that our estimates are only lower limits on the TDE and captured EMRI rates at $z \sim 5$. In particular, the number densities of NSCs in each of the three SMBH mass bins we considered, Φ_1, Φ_2, and Φ_3, are only lower limits. Moreover, under our LRD paradigm, we do not know the properties of the NSCs, and this is the dominant source of uncertainty in our results.

According to S. Babak et al. (2017), depending on the astrophysical model adopted, the intrinsic EMRI rate can be between a few tens and a few tens of thousands at all redshifts. K. Kritos et al. (2025a) find a total of a few thousand captured EMRIs up to $z = 10$. Moreover, the future Laser Interferometer Space Antenna (LISA) is unlikely to be able to detect EMRIs with primary in the range $10^7\,M_\odot$–$10^8\,M_\odot$ and at the redshifts where the majority of the LRDs are observed (S. Babak et al. 2017). However, a gravitational-wave background of EMRIs, i.e., the cumulative gravitational-wave signal from all LRD sources, may still be observable at μHz frequencies.

Comparison with previous work highlights both methodological and physical differences. B. Rom et al. (2024) find that black holes develop a steady-state density profile scaling as r^{-4} within the radius of influence, which becomes shallower as $r^{-1.75}$ at smaller radii, while stars follow slopes of $r^{-1.5}$ closer to the supermassive black hole. Their framework predicts thousands of detectable EMRIs with LISA. In contrast, in our study the power-law slopes are treated as free parameters (see the Appendix), and if EMRIs are expected to outnumber direct plunges, our estimates may represent a lower limit. Similarly, B. Rom & R. Sari (2025) derives cusp slopes of 1.75 for black holes and 1.5 for lighter stars based on analytic arguments, whereas our adopted values of 1.5 and 1.0, respectively, imply reduced rates compared to steady-state predictions. Semianalytic Fokker–Planck estimates of compact object influxes are presented by K. Kaur et al. (2025), while I. Linial & R. Sari (2022) incorporate a mass spectrum and show that, in a steady state, each mass group satisfies a zero-energy-flow solution. A comprehensive comparison with these approaches is beyond the scope of this work. Moreover, we do not compute EMRI rates here and instead focus exclusively on direct plunges.

6. Why are the X-Ray Luminosities Low?

In general, LRDs are subluminous in X-rays (T. T. Ananna et al. 2024; A. Sacchi & A. Bogdan 2025). This superficially is a problem, especially because of the phases we invoke of super-Eddington accretion onto the central BH. Explanations in the literature include an inhomogeneous broad emission-line region with high covering factor (R. Maiolino et al. 2025). F. Pacucci & R. Narayan (2024) consider mildly Eddington accretion rates, which results in lower SMBH masses (see also E. Lambrides et al. 2026). An analogy with ultraluminous X-ray sources, which have highly beamed x-ray emission from super-Eddington accretion onto the central BH, provides yet another interpretation (A. King 2024). P. Madau & F. Haardt (2024) discuss X-ray scattering from the funnel walls, a model that we develop further below.

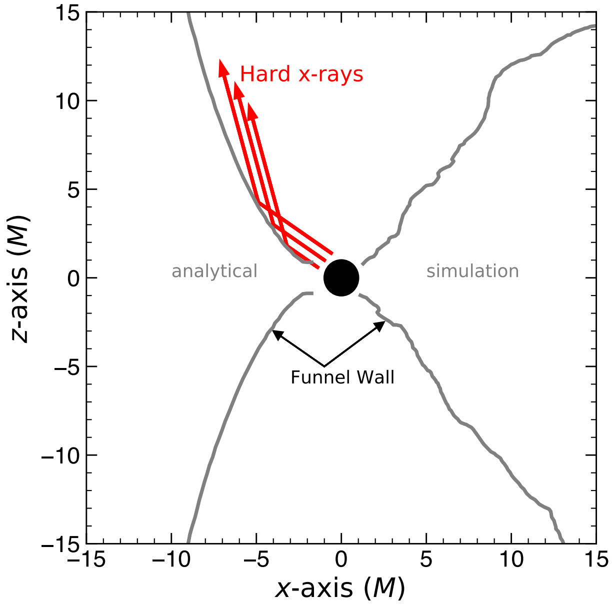

Figure 6. Hard X-rays from the BH hot inner corona scattered on Polish donut funnel walls. The funnel model and thick accretion disk are from analytical (left) and numerical simulations (right) (the values of the envelope are digitized from Figure 1 of Q. Lei et al. 2009 in units of gravitational radii). Scattering of hard X-rays is depicted for the proxy model of Cygnus X-3 (A. Veledina et al. 2024).

We can use Cygnus X-3 as a template for the observability, or lack thereof, of X-rays from the SMBH. Cygnus X-3 is a microquasar produced by a super-Eddington X-ray binary. The central X-ray source is hidden behind the optically thick accretion disk. The narrow disk funnel scatters hard X-rays from the central BH at a source inclination of $\sim 30^\circ$, as measured by the unexpectedly high (12%) X-ray polarization as measured by IXPE (A. Veledina et al. 2024). Due to transient funnel-filling phases of variable accretion, the resulting luminous ultrasoft X-ray flux ionizes the accretion disk corona.

We argue that a very similar phenomenon applies in the super-Eddington phase of the LRD (Q. Lei et al. 2009). There is a deep funnel surrounding the BH in the super-Eddington accretion-induced phase (see Figure 6). This is the so-called Polish donut (P. Madau 2026), which alternates with a slim disk as the accretion rate varies from high to low. The super-Eddington phases are intermittent and brief. They result in intense hard X-rays that are, however, scattered in the funnel. One consequence is that they are viewed only at an oblique angle. Hence, strong X-ray sources associated with super-Eddington accretion are not directly observed in the direction of the LRD in this phase. The soft X-ray component escapes directly and plays a role in ionizing the accretion disk corona. Observational consequences would include unassociated X-ray sources and high X-ray polarization as high as 10%–20% by analogy with Cygnus X-3 (A. Veledina et al. 2024).

7. Conclusions

Regardless of interpretation, LRDs must inevitably host a massive BH; even in the stars-only scenario, the inferred stellar densities are so high that a massive object would rapidly form through runaway stellar collisions (A. Escala et al. 2025; F. Pacucci et al. 2025).

If a significant amount of gas is present in the center of LRDs (G. C. Jones et al. 2025b), EMRIs may be accelerated by the enhanced dynamical friction from the gas environment. As demonstrated by L. Speri et al. (2023), the associated gravitational-wave dephasing imprinted in the gravitational waveform signal may be detectable by LISA.

We found that a significant mass of the SMBH in LRDs could be assembled through the accretion of stars and stellar-mass BHs from the surrounding dense NSC environment. See also N. C. Stone et al. (2017), H. Pfister et al. (2021), F. P. Rizzuto et al. (2023), and M. Polkas et al. (2024) for similar conclusions. High stellar densities increase the rates of TDEs and EMRIs (F. Zhang & P. A. Seoane 2025). The gas further boosts the growth. In the densest system simulated, the IMBH seed rapidly grew through TDEs, EMRIs, and gas accretion within a few tens of Myr. This allows enough time for the BH to grow and the properties of the system to resemble those of LRDs by $z \sim 5$.

In the densest systems, an IMBH seed would rapidly grow through TDEs, EMRIs, and gas accretion. Simulations we carried out for NSCs with a central density of $10^8\,\mathrm{pc}^{-3}$ resulted in the rapid growth of a $10^3\,M_\odot$ IMBH seed into the SMBH regime (final mass $\simeq 2 \times 10^7\,M_\odot$) within a few $\times 10$ Myr, giving rise to the $z \sim 5$ population of LRDs. Again, a significant fraction of the SMBH's mass ($\sim$80%) is assembled through TDEs and captured EMRIs. Note that this fraction is dependent on the mass of the gas reservoir, which is taken in this example to be $10^7\,M_\odot$ and supplied in ten inflow episodes over a 100 Myr period. Moreover, there is a residual population of stellar-mass BHs around the SMBH, leading to subsequent high-energy phenomena such as BH mergers and EMRIs.

While the central massive BH is in the active accretion phase, such a gas-rich NSC with an accreting SMBH in its center would observationally resemble an LRD (K. Inayoshi & R. Maiolino 2025). After the residual gas is removed due to feedback and gas accretion shuts off, the BH becomes quiet. During the inactive phase, though, the BH continues to grow via successive TDEs and EMRIs. J. Bellovary (2025) finds a high-redshift TDE rate of $\sim 10^{-4}\,\mathrm{yr}^{-1}$ by fitting the observed abundance of LRDs to the theoretical number density of SMBH seeds under the assumption that the emission of LRDs is exclusively powered by TDEs. While this rate estimate is five orders of magnitude lower than ours, it cannot explain the necessary growth rate of the BHs. In this paper we envision that the emission of LRDs is dominated by the AGN and gas accretion plays an important role in the growth of BHs.

Using JWST data, M. Karmen et al. (2025) claim a candidate for a high-redshift TDE at $z \approx 5$. Moreover, M. J. Graham et al. (2025) have identified the superluminous optical flare J2245+3743, most likely corresponding to the tidal disruption of a massive ($\gtrsim 10\,M_\odot$) star by a $\sim 3 \times 10^8\,M_\odot$ SMBH at redshift $z \approx 2$. Based on this single observation, M. J. Graham et al. (2025) infer the rate of high-redshift ($z \sim 2$) TDEs to be $\sim 3 \times 10^{-13}\,\mathrm{yr}^{-1}\,\mathrm{Mpc}^{-3}$. This is contrasted with our predicted range 6×10^{-13}–$2 \times 10^{-11}\,\mathrm{yr}^{-1}\,\mathrm{Mpc}^{-3}$ for the $z = 4$–6 TDE rate density. For comparison, according to S. van Velzen & G. R. Farrar (2014), the local TDE rate density is $\sim 3 \times 10^{-7}\,\mathrm{yr}^{-1}\,\mathrm{Mpc}^{-3}$, which is a factor of $\sim$10 less than what theoretical models predict for $z \sim 0$ (N. C. Stone & B. D. Metzger 2016). At the time of writing, five other TDE candidates have been identified at $z > 1$ (Y. Gu et al. 2025). We expect that future experiments, such as UVEX (S. R. Kulkarni et al. 2021), will utilize imaging and spectroscopy to identify many more TDE candidates. Other diagnostics that are currently inconclusive but are expected to rapidly improve include radio detectability (M. A. Latif et al. 2025; K. Perger et al. 2025) and variability (L. J. Furtak et al. 2025; W. L. Tee et al. 2025; S. Zhou et al. 2025).

As the gas is being ejected away from the episodic accretion feedback or gets converted into stars in subsequent starburst episodes, the galaxy builds up its stellar population and eventually starves of gas, limiting SMBH growth through accretion (J. Silk et al. 2024). Thus, some SMBHs may have grown faster than the stellar population around them (I. Juodžbalis et al. 2026), and therefore the $M_{\mathrm{BH}}/M_\star$ ratios are larger at higher redshifts (S. Geris et al. 2025; B. L. Jones et al. 2025a).

The population of stellar-mass BHs around the SMBH in LRDs can lead to other electromagnetic counterparts, such as micro-TDEs (H. B. Perets et al. 2016; K. Kremer et al. 2019; S. Rastello et al. 2026). These involve the tidal disruption of a main-sequence star by a stellar-mass BH. If a population of stellar-mass BHs is present around SMBHs in LRDs, a fraction of stars will be tidally disrupted by BH remnants. This is very likely due to the evolution of massive stars ($\gtrsim 20\,M_\odot$) into BHs in the dense NSC environment. Moreover, there might be other types of high-energy phenomena such as white dwarf tidal disruptions, mergers involving neutron stars, and stellar collisions, all of which produce multimessenger signals.

Preferential gas accretion onto the secondary in an SMBH merger is argued to inevitably boost the SMBH merger rate (M. G. H. Krause et al. 2025), reconciling the pulsar timing array signal with the predicted merger rate at low redshift (A. Toubiana et al. 2025), and providing potentially even more significant boosts in the merger rate predicted in the gas-rich regime, which is characteristic of the high-redshift regime that LISA is expected to probe (J. M. Comerford & J. Simon 2025).

Given the uncertainties of LRD number densities and the unknown properties of their putative central NSCs, we make predictions of intrinsic TDE and captured EMRI rates at $z = 4$–6 with median values of $\sim 500\,\mathrm{yr}^{-1}$ and $\sim 4\,\mathrm{yr}^{-1}$, respectively, depending on the properties of the LRD's NSCs. The values of LRD number density we used from J. Matthee et al. (2024) are lower bounds of the number density of SMBHs. Together with selection effects—the fact that lower-mass SMBHs are more challenging to observe—we conclude that our estimates can only be a lower bound. We may not be able to see individual EMRIs from LRDs at those high redshifts, but we may be able to identify a background of EMRIs instead (M. Bonetti & A. Sesana 2020).

Acknowledgments

We thank Mitch Begelman, Jillian Bellovary, Emanuele Berti, Francesco Bollati, Mitchell Karmen, Piero Madau, Colin Norman, Massimo Ricotti, and Marta Volonteri for discussions. We also thank Daniel D'Orazio, Brenna Mockler, Connar Rowan, Johan Samsing, Mattia Sormani, James Stone, Christofer Tiede, and Alessandro A. Trani for discussions that took place during the NBIA Workshop on Open Problems in Astrophysical Dynamics. Finally, we thank the anonymous referee for their comments. K.K. is supported by NSF grants No. AST-2307146, PHY-2513337, PHY-090003, and PHY-20043, by NASA grant No. 21-ATP21-0010, by John Templeton Foundation Grant No. 62840, by the Simons Foundation [MPS-SIP-00001698, E.B.], by the Simons Foundation International, by Italian Ministry of Foreign Affairs and International Cooperation grant No. PGR01167, and by the Onassis Foundation—Scholarship ID: F ZT 041-1/2023-2024.

Appendix
Dependence on the Cusp Slope

In this Appendix, we explore the dependence of our results on the choice of cusp indices $\alpha_{1,2}$. To isolate its effect, we fix all other parameters, taking $\beta_1 = \beta_2 = -5$, $M_1(t = 0) = 20M_2(t = 0) = 10^6\,M_\odot$, $R_1(t = 0) = 2R_2(t = 0) = 1$ pc. We vary only the indices, for which we further assume $\alpha_1 = \alpha_2 \in \{0.0, -0.5, -1.0, -1.5\}$, and consider five seed BH masses $M_{\rm BH} \in \{10^2, 10^3, 10^4, 10^5, 10^6\}\,M_\odot$; we do not attempt a comprehensive survey of the parameter space in this work. The dependence of the results on the slope of the inner cusp is shown in Figure 7.

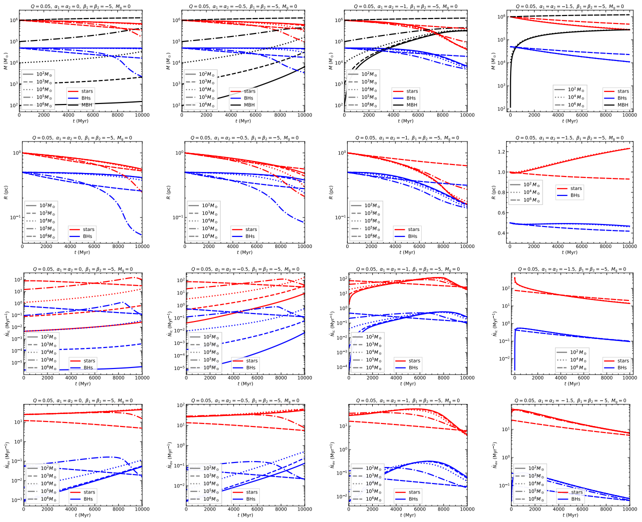

Figure 7. Temporal evolution of the masses (M, top row), radii (R, second row), loss-cone ($\dot{N}_{\rm lc}$, third row), and evaporation rates ($\dot{N}_{\rm ev}$, bottom row) while varying the seed mass of the central growing BH (black lines, top row). We assume stars and stellar-mass BHs have the same inner cusp slopes $\alpha_1 = \alpha_2$, and different columns consider different index values: $\alpha_1 = 0$ (left column), $\alpha_1 = -0.5$ (second column), $\alpha_1 = -1.0$ (third column), and $\alpha_1 = -1.5$ (right column). All other parameters of the model have been fixed. Here Q is the ratio of total mass in stellar-mass BHs ($m_2 = 10\,M_\odot$) to the total mass in low-mass stars ($m_1 = 1\,M_\odot$).

ORCID iDs

Konstantinos Kritos https://orcid.org/0000-0002-0212-3472
Joseph Silk https://orcid.org/0000-0002-1566-8148

References

Adamo, A., Bradley, L. D., Vanzella, E., et al. 2024, Natur, 632, 513
Alexander, T., & Hopman, C. 2009, ApJ, 697, 1861
Ananna, T. T., Bogdán, A., Kovács, O. E., Natarajan, P., & Hickox, R. C. 2024, ApJL, 969, L18
Babak, S., Gair, J., Sesana, A., et al. 2017, PhRvD, 95, 103012
Baggen, J. F. W., van Dokkum, P., Brammer, G., et al. 2024, ApJL, 977, L13
Bardeen, J. M. 1970, Natur, 226, 64
Begelman, M. C., & Dexter, J. 2025, ApJ, 996, 48
Bellovary, J. 2025, ApJL, 984, L55
Bonetti, M., & Sesana, A. 2020, PhRvD, 102, 103023
Bonoli, S., Izquierdo-Villalba, D., Spinoso, D., et al. 2025, arXiv:2509.12325
Casey, C. M., Akins, H. B., Shuntov, M., et al. 2024, ApJ, 965, 98
Choksi, N., Volonteri, M., Colpi, M., Gnedin, O. Y., & Li, H. 2019, ApJ, 873, 100
Chon, S., & Omukai, K. 2025, MNRAS, 539, 2561
Comerford, J. M., & Simon, J. 2025, ApJ, 994, 168
de Graaff, A., Rix, H.-W., Naidu, R. P., et al. 2025, A&A, 701, A168
Dokuchaev, V. I. 1991, MNRAS, 251, 564
Escala, A. 2021, ApJ, 908, 57
Escala, A., Zimmermann, L., Valdebenito, S., et al. 2025, Astrophys.J., 995, 44
Fahrion, K., Bulichi, T.-E., Hilker, M., et al. 2022, A&A, 667, A101
Frank, J., & Rees, M. J. 1976, MNRAS, 176, 633
Furtak, L. J., Secunda, A. R., Greene, J. E., et al. 2025, A&A, 698, A227
Garcia, F. A. B., Ricotti, M., & Sugimura, K. 2025, OJAp, 8, 146
Geris, S., Maiolino, R., Isobe, Y., et al. 2025, MNRAS, 545, staf1979
Gezari, S. 2021, ARA&A, 59, 21
Goodman, J., & Hut, P. 1993, ApJ, 403, 271
Graham, M. J., et al. 2025, NatAs, 10, 154
Greene, J. E., Labbe, I., Goulding, A. D., et al. 2024, ApJ, 964, 39
Greene, J. E., Strader, J., & Ho, L. C. 2020, ARA&A, 58, 257
Gu, Y., Zhang, X.-G., Chen, X.-Q., Yang, X., & Liang, E.-W. 2025, MNRAS, 537, 84
Guo, M., Stone, J. M., Quataert, E., & Springel, V. 2025, ApJ, 987, 202
Henshaw, J. D., Barnes, A. T., Battersby, C., et al. 2023, ASPC, 534, 83
Hills, J. G. 1980, ApJ, 235, 986
Inayoshi, K. 2025, ApJ, 988, L22
Inayoshi, K., & Maiolino, R. 2025, ApJL, 980, L27
Inayoshi, K., Murase, K., & Kashiyama, K. 2025, ApJ, 1000, 90
Inayoshi, K., Visbal, E., & Haiman, Z. 2020, ARA&A, 58, 27
Ji, X., Maiolino, R., Übler, H., et al. 2025, MNRAS, 544, 3900
Jones, B. L., Kocevski, D. D., Pacucci, F., et al. 2025a, arXiv:2510.07376
Jones, G. C., Übler, H., Maiolino, R., et al. 2025b, MNRAS, 546, stag115
Juodžbalis, I., Maiolino, R., Baker, W. M., et al. 2024, Natur, 636, 594
Juodžbalis, I., Maiolino, R., Baker, W. M., et al. 2025, MNRAS, 546, stag086
Juodžbalis, I., Marconcini, C., D'Eugenio, F., et al. 2026, Natur, 653, 1017
Karmen, M., Gezari, S., Lambrides, E., et al. 2025, ApJ, 990, 149
Kaur, K., Rom, B., & Sari, R. 2025, ApJ, 980, 150
King, A. 2024, MNRAS, 531, 550
Kovacs, O. E., Bogdán, Á., Natarajan, P., et al. 2024, ApJL, 965, L21
Krause, M. G. H., Bourne, M. A., Britzen, S., et al. 2025, PASA, 42, e162
Kremer, K., Lu, W., Rodriguez, C. L., Lachat, M., & Rasio, F. 2019, ApJ, 881, 75
Kritos, K., Beckmann, R. S., Silk, J., et al. 2025a, Astrophys.J., 991, 58
Kritos, K., Berti, E., & Silk, J. 2023, PhRvD, 108, 083012
Kritos, K., Berti, E., & Silk, J. 2024a, MNRAS, 531, 133
Kritos, K., Reali, L., Gerosa, D., & Berti, E. 2024b, PhRvD, 110, 123017
Kritos, K., Reali, L., Ng, K. K. Y., Antonini, F., & Berti, E. 2025b, PhRvD, 111, 063056
Kulkarni, S. R., Harrison, A., Grefenstette, B. W., et al. 2021, arXiv:2111.15608
Labbé, I., van Dokkum, P., Nelson, E., et al. 2023, Natur, 616, 266
Lahén, N., Naab, T., Rantala, A., & Partmann, C. 2025, MNRAS, 543, 1023
Lambrides, E., Larson, R., Garofali, K., et al. 2026, NatAs, in press
Latif, M. A., Aftab, A., Whalen, D. J., & Mezcua, M. 2025, A&A, 694, L14
Lauer, T. R., Ajhar, E. A., Byun, Y. I., et al. 1995, AJ, 110, 2622
Lei, Q., Abramowicz, M. A., Fragile, P. C., et al. 2009, A&A, 498, 471
Lin, X., Fan, X., Cai, Z., et al. 2025, ApJ, 997, 364
Linial, I., & Sari, R. 2022, ApJ, 940, 101
Loiacono, F., Gilli, R., Mignoli, M., et al. 2025, A&A, 703, A36
Madau, P. 2026, A&A, 708, A116
Madau, P., & Haardt, F. 2024, ApJL, 976, L24
Maiolino, R., Risaliti, G., Signorini, M., et al. 2025, MNRAS, 538, 1921
Maiolino, R., Scholtz, J., Curtis-Lake, E., et al. 2024a, A&A, 691, A145
Maiolino, R., Scholtz, J., Witztok, J., et al. 2024b, Natur, 627, 59
Maiolino, R., Uebler, H., D'Eugenio, F., et al. 2026, MNRAS, 548, staf2109
Matthee, J., Naidu, R. P., Brammer, G., et al. 2024, ApJ, 963, 129
Mayer, L., van Donkelaar, F., Messa, M., Capelo, P. R., & Adamo, A. 2025, ApJL, 981, L28

McClymont, W., Tacchella, S., Ji, X., et al. 2026, MNRAS, 545, staf2092
Merritt, D. 2013, Dynamics and Evolution of Galactic Nuclei (Princeton Univ. Press)
Mouri, H., & Taniguchi, Y. 2002, ApJL, 566, L17
Mowla, L., Iyer, K., Asada, Y., et al. 2024, Natur, 636, 332
Mummery, A. 2023, MNRAS, 527, 6233
Naidu, R. P., Matthee, J., Katz, H., et al. 2025, arXiv:2503.16596
Neumayer, N., Seth, A., & Boeker, T. 2020, A&ARv, 28, 4
O'Leary, R. M., Kocsis, B., & Loeb, A. 2009, MNRAS, 395, 2127
Pacucci, F., Hernquist, L., & Fujii, M. 2025, Astrophys.J., 994, 40
Pacucci, F., & Narayan, R. 2024, ApJ, 976, 96
Panamarev, T., Just, A., Spurzem, R., et al. 2019, MNRAS, 484, 3279
Perets, H. B., Hopman, C., & Alexander, T. 2007, ApJ, 656, 709
Perets, H. B., Li, Z., Lombardi, J. C., & Milcarek, S. R. 2016, ApJ, 823, 113
Perger, K., Fogasy, J., Frey, S., & Gabányi, K. É. 2025, A&A, 693, L2
Pfister, H., Dai, J. L., Volonteri, M., et al. 2021, MNRAS, 500, 3944
Polak, B., Mac Low, M.-M., Klessen, R. S., et al. 2024, A&A, 690, A94
Polkas, M., Bonoli, S., Bortolas, E., et al. 2024, A&A, 689, A204
Poutanen, J., Fabrika, S., Butkevich, A. G., & Abolmasov, P. 2007, MNRAS, 377, 1187
Quinlan, G. D., & Shapiro, S. L. 1989, ApJ, 343, 725
Rantala, A., & Naab, T. 2025, MNRASL, 542, L78
Rantala, A., Naab, T., & Lahén, N. 2024, MNRAS, 531, 3770
Rastello, S., Iorio, G., Gieles, M., & Wang, L. 2026, A&A, 707, A217
Rees, M. J. 1988, Natur, 333, 523
Reynolds, C. S. 2021, ARA&A, 59, 117
Ricarte, A., & Natarajan, P. 2018, MNRAS, 481, 3278
Rizzuto, F. P., Naab, T., Rantala, A., et al. 2023, MNRAS, 521, 2930
Rodriguez, C. L., Chatterjee, S., & Rasio, F. A. 2016, PhRvD, 93, 084029
Rom, B., Linial, I., Kaur, K., & Sari, R. 2024, ApJ, 977, 7
Rom, B., & Sari, R. 2025, ApJ, 991, 146
Rose, S. C., & MacLeod, M. 2024, ApJL, 963, L17
Rose, S. C., Naoz, S., Sari, R., & Linial, I. 2023, ApJ, 955, 30
Rozner, M., & Ramirez-Ruiz, E. 2025, ApJL, 988, L21
Sacchi, A., & Bogdan, A. 2025, ApJL, 989, L30
Schödel, R., Feldmeier, A., Kunneriath, D., et al. 2014, A&A, 566, A47
Schödel, R., Merritt, D., & Eckart, A. 2009, A&A, 502, 91
Shapiro, S. L. 1977, ApJ, 217, 281
Shlosman, I., Begelman, M. C., & Frank, J. 1990, Natur, 345, 679
Shlosman, I., Frank, J., & Begelman, M. C. 1989, Natur, 338, 45
Silk, J., Begelman, M. C., Norman, C., Nusser, A., & Wyse, R. F. G. 2024, ApJL, 961, L39
Sormani, M. C., Barnes, A. T., Sun, J., et al. 2023, MNRAS, 523, 2918
Speri, L., Antonelli, A., Sberna, L., et al. 2023, PhRvX, 13, 021035
Stone, N. C., Küpper, A. H. W., & Ostriker, J. P. 2017, MNRAS, 467, 4180
Stone, N. C., & Metzger, B. D. 2016, MNRAS, 455, 859
Syer, D., & Ulmer, A. 1999, MNRAS, 306, 35
Tee, W. L., Fan, X., Wang, F., & Yang, J. 2025, ApJL, 983, L26
Toubiana, A., Sberna, L., Volonteri, M., et al. 2025, A&A, 700, A135
van Donkelaar, F., Mayer, L., Capelo, P. R., et al. 2024, MNRAS, 529, 4104
van Velzen, S., & Farrar, G. R. 2014, ApJ, 792, 53
Vanzella, E., Claeyssens, A., Welch, B., et al. 2023, ApJ, 945, 53
Veledina, A., Poutanen, J., Bocharova, A., et al. 2024, A&A, 688, L27
Vergara, M. C., Askar, A., Flammini Dotti, F., et al. 2025, A&A, 707, A71
Vergara, M. C., Escala, A., Schleicher, D. R. G., & Reinoso, B. 2023, MNRAS, 522, 4224
Wang, B., Leja, J., Katz, H., et al. 2025, ApJ, 1003, 10
Williams, C. E., Naoz, S., Lake, W., et al. 2025, ApJ, 990, 135
Zana, T., Capelo, P. R., Boresta, M., et al. 2026, Astron.Astrophys. , 708, A7
Zhang, F., & Seoane, P. A. 2025, ApJ, 999, 224
Zhang, L., Stone, J. M., Mullen, P. D., et al. 2025, ApJ, 995, 26
Zhou, S., Sun, M., Zhang, Z., Chen, J., & Ho, L. C. 2025, ApJ, 991, 137
Zhou, Y., & Zhong, X. G. 1990, Ap&SS, 168, 233
Zwick, L., Tiede, C., & Mayer, L. 2026, ApJ, 1002, 7